

**GEORGIA DOT RESEARCH PROJECT 18-27**

**Final Report**

**CONTINUOUS FIELD VALIDATION OF A  
WIRELESS STRUCTURAL MONITORING  
AND BRIDGE WEIGH-IN-MOTION (BWIM)  
SYSTEM**



**Office of Performance-based Management and Research**  
600 West Peachtree Street NW | Atlanta, GA 30308

**January 2022**

## TECHNICAL REPORT DOCUMENTATION PAGE

1. Report No. FHWA-GA-22-1827	2. Government Accession No. N/A	3. Recipient's Catalog No. N/A	
4. Title and Subtitle Continuous Field Validation of a Wireless Structural Monitoring and Bridge Weigh-In-Motion (BWIM) System		5. Report Date Jan 2022	
		6. Performing Organization Code N/A	
7. Authors Peter Lander ( <a href="https://orcid.org/0000-0002-5661-7953">https://orcid.org/0000-0002-5661-7953</a> ); Yang Wang, Ph.D. ( <a href="https://orcid.org/0000-0002-1031-9491">https://orcid.org/0000-0002-1031-9491</a> )		8. Performing Organization Report No. 18-27	
9. Performing Organization Name and Address Georgia Institute of Technology 790 Atlantic Drive Atlanta, GA 30332		10. Work Unit No. N/A	
		11. Contract or Grant No. PI#0015718	
12. Sponsoring Agency Name and Address Georgia Department of Transportation Office of Performance-based Management and Research 600 West Peachtree Street NW Atlanta, GA 30308		13. Type of Report and Period Covered Final Report Oct 2018 – Jan 2022	
		14. Sponsoring Agency Code N/A	
15. Supplementary Notes Prepared in cooperation with the U.S. Department of Transportation, Federal Highway Administration.			
16. Abstract This report details the implementation of a wireless structural monitoring and bridge weigh-in-motion system. The goal of the project is to develop, install, and maintain a wireless structural monitoring system to perform long-term bridge weigh-in-motion. The developed system adopts the <i>Martlet</i> wireless sensing system for data collection and monitoring. Advancements to the <i>Martlet</i> system were made so that each wireless node is powered with energy harvested from solar panels. This is achieved by developing power-saving methods that allow the sensors to sleep when they are not actively capturing the bridge response to a passing truck. To detect passing trucks, distance-measuring LIDAR sensors are used in parallel with strain transducers mounted to the underside of the bridge deck. The developed system was installed at an in-service interstate highway bridge that carries the two southbound lanes of I-85 over Georgia State Route 109, outside of the city of LaGrange. <i>Martlet</i> sensing nodes were placed at the third points on the two middle bridge spans. The nodes can collect acceleration, strain, and temperature data. Controlled testing was performed on the bridge using a loaded dump truck with known axle weights. The data collected from the testing are used to validate the system's effectiveness at performing bridge weigh-in-motion. Following the controlled testing, the system was put into a long-term operational mode, where data are collected automatically as trucks cross the bridge. These data are then stored in the cloud, where they can be accessed to perform monitoring and bridge weigh-in-motion.			
17. Key Words Weigh in motion, wireless sensors, wireless sensor networks, structural health monitoring, highway bridges, detection and identification systems		18. Distribution Statement No restrictions. This document is available through the National Technical Information Service, Springfield, VA 22161.	
19. Security Classification (of this report) Unclassified	20. Security Classification (of this page) Unclassified	21. No. of Pages 57	22. Price Free

GDOT Research Project 18-27

Final Report

CONTINUOUS FIELD VALIDATION OF A WIRELESS STRUCTURAL  
MONITORING AND BRIDGE WEIGH-IN-MOTION (BWIM) SYSTEM

By

Peter Lander

Graduate Research Assistant, School of Civil and Environmental Engineering  
Georgia Institute of Technology

and

Yang Wang, Ph.D.

Professor, School of Civil and Environmental Engineering and  
School of Electrical and Computer Engineering  
Georgia Institute of Technology

Georgia Tech Research Corporation

Contract with  
Georgia Department of Transportation

In cooperation with  
U.S. Department of Transportation  
Federal Highway Administration

January 2022

The contents of this report reflect the views of the authors, who are responsible for the facts and accuracy of the data presented herein. The contents do not necessarily reflect the official views or policies of the Georgia Department of Transportation or the Federal Highway Administration. This report does not constitute a standard, specification, or regulation.

# SI\* (MODERN METRIC) CONVERSION FACTORS

## APPROXIMATE CONVERSIONS TO SI UNITS

Symbol	When You Know	Multiply By	To Find	Symbol
<b>LENGTH</b>				
in	inches	25.4	millimeters	mm
ft	feet	0.305	meters	m
yd	yards	0.914	meters	m
mi	miles	1.61	kilometers	km
<b>AREA</b>				
in <sup>2</sup>	square inches	645.2	square millimeters	mm <sup>2</sup>
ft <sup>2</sup>	square feet	0.093	square meters	m <sup>2</sup>
yd <sup>2</sup>	square yard	0.836	square meters	m <sup>2</sup>
ac	acres	0.405	hectares	ha
mi <sup>2</sup>	square miles	2.59	square kilometers	km <sup>2</sup>
<b>VOLUME</b>				
fl oz	fluid ounces	29.57	milliliters	mL
gal	gallons	3.785	liters	L
ft <sup>3</sup>	cubic feet	0.028	cubic meters	m <sup>3</sup>
yd <sup>3</sup>	cubic yards	0.765	cubic meters	m <sup>3</sup>
NOTE: volumes greater than 1000 L shall be shown in m <sup>3</sup>				
<b>MASS</b>				
oz	ounces	28.35	grams	g
lb	pounds	0.454	kilograms	kg
T	short tons (2000 lb)	0.907	megagrams (or "metric ton")	Mg (or "t")
<b>TEMPERATURE (exact degrees)</b>				
°F	Fahrenheit	5 (F-32)/9 or (F-32)/1.8	Celsius	°C
<b>ILLUMINATION</b>				
fc	foot-candles	10.76	lux	lx
fl	foot-Lamberts	3.426	candela/m <sup>2</sup>	cd/m <sup>2</sup>
<b>FORCE and PRESSURE or STRESS</b>				
lbf	poundforce	4.45	newtons	N
lbf/in <sup>2</sup>	poundforce per square inch	6.89	kilopascals	kPa

## APPROXIMATE CONVERSIONS FROM SI UNITS

Symbol	When You Know	Multiply By	To Find	Symbol
<b>LENGTH</b>				
mm	millimeters	0.039	inches	in
m	meters	3.28	feet	ft
m	meters	1.09	yards	yd
km	kilometers	0.621	miles	mi
<b>AREA</b>				
mm <sup>2</sup>	square millimeters	0.0016	square inches	in <sup>2</sup>
m <sup>2</sup>	square meters	10.764	square feet	ft <sup>2</sup>
m <sup>2</sup>	square meters	1.195	square yards	yd <sup>2</sup>
ha	hectares	2.47	acres	ac
km <sup>2</sup>	square kilometers	0.386	square miles	mi <sup>2</sup>
<b>VOLUME</b>				
mL	milliliters	0.034	fluid ounces	fl oz
L	liters	0.264	gallons	gal
m <sup>3</sup>	cubic meters	35.314	cubic feet	ft <sup>3</sup>
m <sup>3</sup>	cubic meters	1.307	cubic yards	yd <sup>3</sup>
<b>MASS</b>				
g	grams	0.035	ounces	oz
kg	kilograms	2.202	pounds	lb
Mg (or "t")	megagrams (or "metric ton")	1.103	short tons (2000 lb)	T
<b>TEMPERATURE (exact degrees)</b>				
°C	Celsius	1.8C+32	Fahrenheit	°F
<b>ILLUMINATION</b>				
lx	lux	0.0929	foot-candles	fc
cd/m <sup>2</sup>	candela/m <sup>2</sup>	0.2919	foot-Lamberts	fl
<b>FORCE and PRESSURE or STRESS</b>				
N	newtons	0.225	poundforce	lbf
kPa	kilopascals	0.145	poundforce per square inch	lbf/in <sup>2</sup>

\* SI is the symbol for the International System of Units. Appropriate rounding should be made to comply with Section 4 of ASTM E380. (Revised March 2003)

## TABLE OF CONTENTS

<b>EXECUTIVE SUMMARY .....</b>	<b>1</b>
<b>INTRODUCTION .....</b>	<b>3</b>
<b>CHAPTER 1. INTERSTATE BRIDGE INSTRUMENTATION .....</b>	<b>4</b>
<b>BRIDGE BACKGROUND INFORMATION.....</b>	<b>4</b>
<b>INSTRUMENTATION OF THE <i>MARTLET</i> WIRELESS SENSING SYSTEM .....</b>	<b>5</b>
<i>Martlet</i> Wireless Sensing System .....	5
Instrumentation Plan.....	7
<b>MODAL HAMMER FIELD TESTING .....</b>	<b>9</b>
Measured Bridge Acceleration Response .....	9
Modal Analysis .....	11
<b>FINITE ELEMENT BRIDGE MODELING .....</b>	<b>13</b>
Finite Element Model Creation .....	13
Comparison of Finite Element Model and As-Built Bridge.....	14
Finite Element Model Updating .....	15
<b>CHAPTER 2. CONTROLLED BWIM FIELD TESTING .....</b>	<b>19</b>
<b>INTRODUCTION .....</b>	<b>19</b>
<b>CONTROL TRUCK DETAILS .....</b>	<b>19</b>
<b>TEST DETAILS AND DATA.....</b>	<b>20</b>
Static Tests .....	21
Dynamic Tests .....	22
Temperature Data.....	24
<b>TRUCK DETECTION WITH LIDAR.....</b>	<b>25</b>
<b>TRUCK DETECTION WITH DECK-MOUNTED STRAIN TRANSDUCERS.....</b>	<b>26</b>
<b>BWIM ANALYSIS .....</b>	<b>28</b>
BWIM Algorithms .....	28

<b>BWIM Results – Simulation .....</b>	<b>29</b>
<b>BWIM Results – Field Testing.....</b>	<b>35</b>
<b>CHAPTER 3. WIRELESS BWIM SYSTEM FIELD DEPLOYMENT .....</b>	<b>38</b>
<b>INTRODUCTION .....</b>	<b>38</b>
<b>SYSTEM DETAILS .....</b>	<b>38</b>
<b>Main Enclosure .....</b>	<b>38</b>
<b>The Gateway .....</b>	<b>40</b>
<b>Solar Energy Harvesting .....</b>	<b>41</b>
<b>Power-Saving Features .....</b>	<b>43</b>
<b>Data Acquisition Triggering via LIDAR .....</b>	<b>44</b>
<b>CONTINUOUS FIELD DATA.....</b>	<b>45</b>
<b>CONCLUSIONS .....</b>	<b>47</b>
<b>ACKNOWLEDGEMENTS .....</b>	<b>48</b>
<b>REFERENCES.....</b>	<b>49</b>

## LIST OF FIGURES

Figure 1. Diagram. Bridge elevation.....	5
Figure 2. Photographs. <i>Martlet</i> wireless sensing system.....	6
Figure 3. Photographs. The integrated accelerometer. ....	6
Figure 4. Diagram. Bridge instrumentation plan. ....	7
Figure 5. Photographs. Sensors installed at the bridge. ....	8
Figure 6. Diagram. Modal analysis hammer hit locations.....	10
Figure 7. Graphs. Hammer impact at location 2B. ....	10
Figure 8. Graphs. Acceleration response of all accelerometers to hammer impact at location 2B.....	11
Figure 9. Diagram. Finite element model of the bridge.....	13
Figure 10. Diagram. Bridge model with updating parameters labeled.....	18
Figure 11. Photo. GDOT dump truck with axle spacings dimensioned. ....	20
Figure 12. Diagram. Dump truck wheel weights.....	20
Figure 13. Diagram. Sensor group labels.....	21
Figure 14. Plots. Left lane static test strain data at select points. ....	22
Figure 15. Plots. Right lane static test strain data at select points. ....	22
Figure 16. Plots. Vertical acceleration at select locations. ....	23
Figure 17. Plots. Bending strain at select locations. ....	24
Figure 18. Plots. Temperature over a few hours at interior beam sensor groups. ....	24
Figure 19. Plots. Surface plot depictions of beam temperature at different times on June 16, 2021. ....	25
Figure 20. Plots. Detection of truck wheels with LIDAR sensors.....	26
Figure 21. Plots. Detection of truck wheels with strain transducers.....	28
Figure 22. Plots. BWIM simulation results for sensors at beam quarter points. ....	32
Figure 23. Plots. BWIM simulation results for sensors at beam third points. ....	33
Figure 24. Plots. BWIM simulation results for sensors at beam half points. ....	34
Figure 25. Plots. BWIM GVW estimation results for Test A. ....	36
Figure 26. Plots. BWIM GVW estimation results for Test B. ....	36
Figure 27. Diagram. BWIM system overview.....	39
Figure 28. Photographs. Main enclosure on Bent 2.....	39
Figure 29. Photographs. <i>Martlet</i> receiver and antenna on Bent 3. ....	41
Figure 30. Photo and schematic. Solar energy harvesting components.....	42
Figure 31. Photographs. Pole-mounted LIDAR sensors.....	45
Figure 32. Plot. BWIM GVW estimate for unknown truck crossing the bridge. ....	46

## LIST OF TABLES

Table 1. Modal analysis results.....	12
Table 2. Mode shape comparison between experimental modal analysis results and the initial FE model.....	12
Table 3. Comparison of natural frequencies for the first six modes. ....	15
Table 4. Comparison of natural frequencies for the updated model. ....	18
Table 5. BWIM simulation estimation results using the FIC estimator. ....	35
Table 6. BWIM results from the experimental field test data. ....	37



## EXECUTIVE SUMMARY

This report details the implementation of a wireless structural monitoring and bridge weigh-in-motion system. The goal of the project is to develop, install, and maintain a wireless structural monitoring system to perform long-term bridge weigh-in-motion. The developed system adopts the *Martlet* wireless sensing system for data collection and monitoring. Advancements to the *Martlet* system were made so that each wireless node is powered with energy harvested from solar panels. Just four small solar panels are needed to power 16 wireless sensing units. This is achieved by developing power-saving methods that allow the sensors to sleep when they are not actively capturing the bridge response to a passing truck. To detect passing trucks, a method of interfacing distance-measuring LIDAR sensors to the *Martlet* wireless nodes was developed. Additionally, it was found that truck detection is possible via strain transducers that are mounted to the underside of the deck in the lanes of travel.

The developed system was installed at an in-service interstate highway bridge. The four-span bridge carries the two southbound lanes of I-85 over Georgia State Route 109, outside of the city of LaGrange. The *Martlet* sensing nodes were placed at the third points on the two middle bridge spans. The nodes capture combinations of vertical acceleration, lateral acceleration, deck strain, beam bending strain, and temperature.

Controlled testing was performed on the bridge using a loaded dump truck with known axle weights. The data collected from the testing are used to validate the system's effectiveness at performing bridge weigh-in-motion. A Finite Input Covariance estimator and a Limited Frequency Bandwidth estimator are selected as the algorithm to perform the weight estimation. The estimators utilize a finite element model of the bridge along with the measured bridge

response to inversely estimate the axle weights of a crossing vehicle. Analysis of the control test data shows that the system has the capability to estimate the gross vehicle weight of trucks with around 5 to 10 percent error.

Following the controlled testing, the system was put into a long-term operation mode, where data are collected automatically as trucks cross the bridge. These data are then stored in the cloud, where they can be accessed to perform monitoring and bridge weigh-in-motion.

## INTRODUCTION

In the U.S. Department of Transportation's (USDOT) 2017 report, *Beyond Traffic 2045*, it is noted that heavy truck traffic is increasing and is expected to continue to increase alongside an increased demand for freight shipments.<sup>[1]</sup> This trend heightens the concern of overloaded vehicles, which pose a threat to roadway and infrastructure safety. Currently, weight enforcement is performed at weigh stations using static scales and sometimes weigh-in-motion (WIM) devices. Traditional weigh stations are inefficient and expensive to maintain. Bridge weigh-in-motion (BWIM) systems use sensors to measure the response of a bridge. By leveraging the latest wireless sensing technology, a BWIM system has the potential to decrease costs and increase the effectiveness of enforcement efforts.

The primary goals of this project are to develop, install, and validate a wireless BWIM system. The *Martlet* wireless sensing system serves as the central technology relied upon to collect the BWIM data.<sup>[2]</sup> To achieve the goals of the project, developments made to the *Martlet* system focused on solar energy harvesting, power efficiency improvements, and truck detection methods. The system was installed on an interstate highway bridge and validated with a controlled truck test. Continuous validation and monitoring of the bridge were performed with a long-term field deployment of the BWIM system.

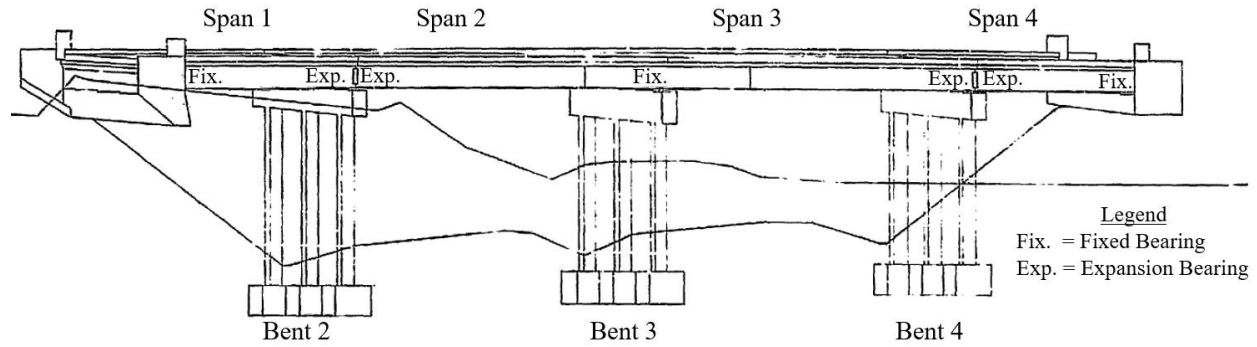
## **CHAPTER 1. INTERSTATE BRIDGE INSTRUMENTATION**

This chapter introduces the bridge and the instrumentation that was utilized for this research project. The chapter begins with a description of the bridge. Next, the sensing system installed on the bridge is introduced. Then, the modal hammer field testing is described, and results are presented. Lastly, the creation of a finite element model is discussed.

### **BRIDGE BACKGROUND INFORMATION**

A bridge in Troup County, Georgia, near the city of LaGrange served as the test structure on which the research presented in this report was performed. The bridge, built in 1977, carries two southbound lanes of Interstate 85 and passes over Georgia State Route (SR) 109. It is located approximately 5 miles south of a weigh station, which makes it a beneficial location for testing BWIM systems. In fact, the bridge was previously instrumented with a cabled monitoring system in 2018 by Pennoni, a consulting engineering firm.

An elevation of the bridge is provided in figure 1. The bridge consists of four spans. The beginning and end spans are simply supported, while the middle two spans are continuous and are longitudinally fixed at the middle bent. All spans consist of W36 steel I-beams that are composite with an 8-inch reinforced concrete deck. For this research, only the middle two spans, Span 2 and Span 3, are instrumented and modeled. It is assumed that negligible interaction exists between the end spans and the middle spans because of the expansion joints separating them.



**Figure 1. Diagram. Bridge elevation.**

## **INSTRUMENTATION OF THE *MARTLET* WIRELESS SENSING SYSTEM**

This section introduces the *Martlet* wireless sensing system and its corresponding sensors.

Additionally, this section describes how the sensors and the sensing system were installed on the bridge.

### ***Martlet* Wireless Sensing System**

The *Martlet* wireless sensing system is a low-cost platform that is designed for smart monitoring of infrastructure. The backbone of the system, shown in figure 2-A, is the *Martlet* motherboard, which features a dual-core Texas Instruments Piccolo microcontroller and a ZigBee radio. The microcontroller can run at speeds up to 90 MHz, and the radio can transmit data at rates up to 250 kbps. The *Martlet* motherboard is designed to be interfaced with other daughterboards to add sensing capabilities.

One such daughterboard utilized in this research was designed to provide high resolution data acquisition via a 24-bit analog-to-digital converter (ADC) chip. This daughterboard, shown in figure 2-B, has been designed with three channels that can be used for either strain or acceleration measurements and one fixed channel for temperature measurement via a thermistor.

The acceleration measurements come from an external sensor named the Integrated

Accelerometer Board, shown in figure 3. Both the strain and acceleration channels have analog low-pass filters with digitally adjustable gains and cutoff frequencies. This adjustability allows the filter to be tuned for a specific structure based on the frequency range being excited and the magnitude of the structure's response.

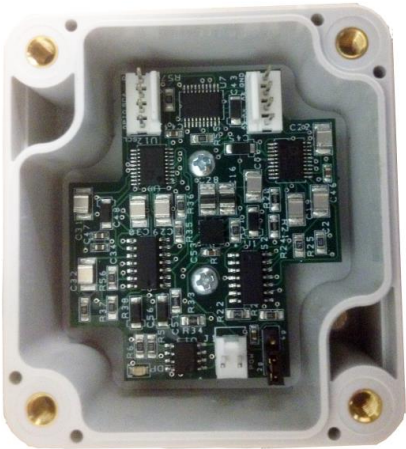


**A. Martlet motherboard.**



**B. 24-bit ADC daughterboard.**

**Figure 2. Photographs. Martlet wireless sensing system.**



**A. Accelerometer circuit board.**

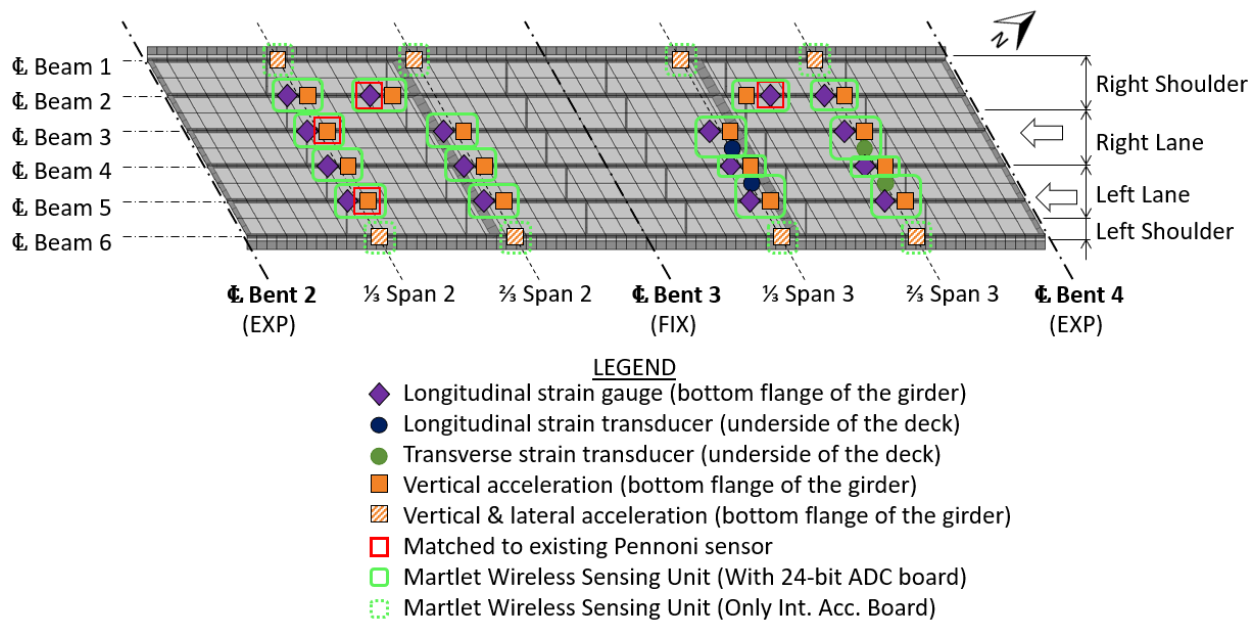


**B. Weatherproof case enclosing the accelerometer board.**

**Figure 3. Photographs. The integrated accelerometer.**

## Instrumentation Plan

To capture the complete response of the bridge, a sensor grid is adopted. The sensor locations, shown in figure 4, are mostly at the span third points, which with two spans and six beams results in 24 *Martlet* wireless sensing units. At each unit there is either an accelerometer or both an accelerometer and a strain gage. These sensors are mounted on the top surface of the bottom flange of the beams, as figure 5-A shows. The accelerometers are mounted with an outdoor adhesive mounting tape and are positioned so that vertical acceleration corresponds to their x-axis and lateral acceleration corresponds to their z-axis. The strain gages are bonded directly to bare steel with cyanoacrylate (superglue) and are positioned parallel to the longitudinal direction of the beams so that they measure the major axis bending strain. At each strain gage location, a thermistor is placed alongside the gage. For protection, the strain gages and thermistors are covered with one layer of butyl rubber sealant and a top layer of neoprene rubber.



**Figure 4. Diagram. Bridge instrumentation plan.**



**A. Integrated accelerometer and covered strain gage.**



**B. Strain transducer.**

**Figure 5. Photographs. Sensors installed at the bridge.**

Additionally, strain transducers are mounted at four locations on the underside of the deck, as is shown in figure 5-B. These sensors are not used to capture the dynamic bridge response. Instead, they are experimentally used to detect truck axles for BWIM from spikes in their signals when wheels pass over them. This is discussed further in chapter 2.

Past BWIM research and simulations for this bridge found that including strain gages and accelerometers on the exterior beams was not necessary; therefore, strain gages are only mounted on the interior beams. Still, the exterior beams were instrumented with accelerometers so that complete mode shapes could be captured. These exterior beam accelerometers are interfaced directly to *Martlet* motherboards, which means their signals are sampled at a resolution of 12 bits. The interior beam *Martlets* are interfaced with the 24-bit ADC daughterboards, allowing for four sensing channels per *Martlet*. The first channel is the vertical acceleration, the second channel is either lateral acceleration or a strain transducer, the third channel is bending strain, and the fourth channel is temperature.



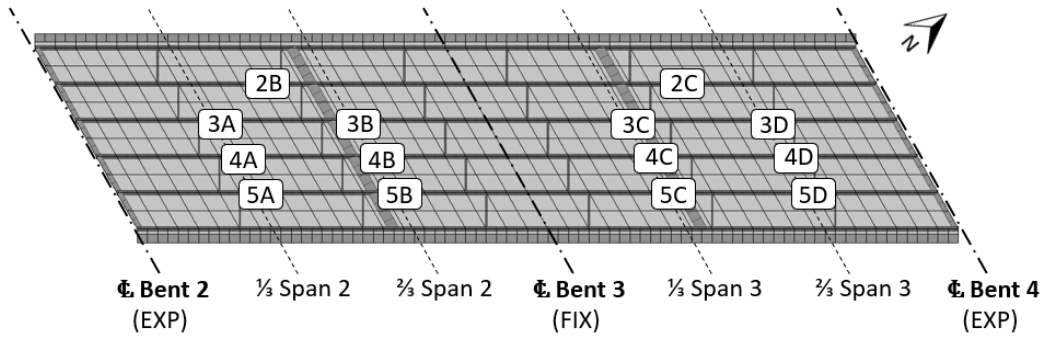
## **MODAL HAMMER FIELD TESTING**

To perform BWIM, an accurate model of the structure is needed. However, a model created from engineering plans will never exactly match the as-built structure. Additionally, for an older structure, deterioration may have affected the structural properties. One approach for determining how the structure is currently behaving is to look at its dynamic properties via modal analysis. These properties include natural frequencies, mode shapes, and damping ratios.

To obtain high-quality dynamic properties, it is beneficial to measure the structure's response to a known input. One way to do this is to use a modal hammer, which excites a range of frequencies. Testing was performed at the bridge on multiple days using a modal hammer. The hammer used was a PCB Piezotronics Model 086D50 large sledge impulse hammer. This hammer has a force sensor that allows for the force imparted by the hammer on the bridge to be measured.

### **Measured Bridge Acceleration Response**

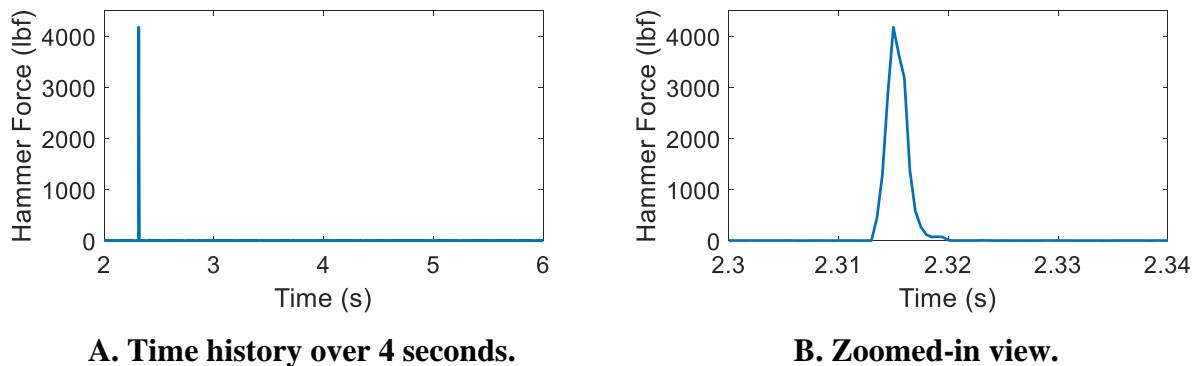
A benefit of using the *Martlet* wireless sensing system for the modal testing was that the modal hammer was wireless, allowing for easy movement to different locations on the bridge deck. To capture the complete response of the bridge, hammer impacts were located along a grid of locations that aligned with the sensor locations. Figure 6 shows the hammer hit locations.



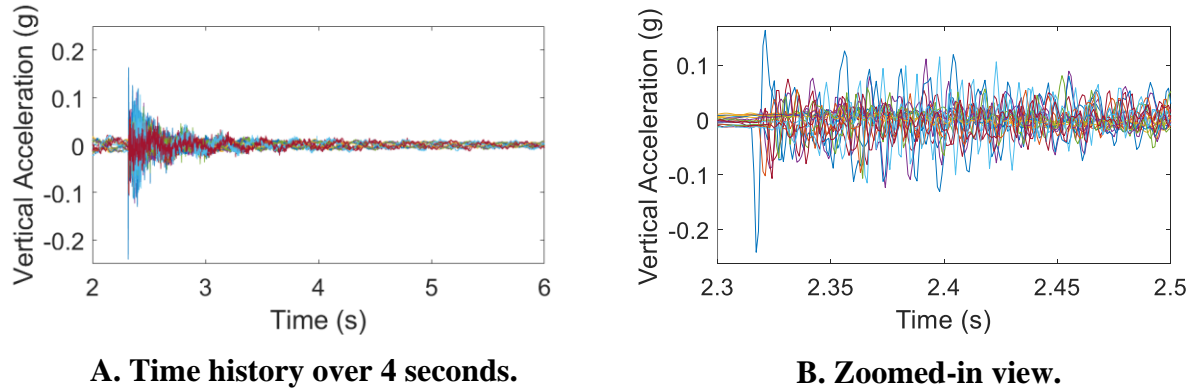
**Figure 6. Diagram. Modal analysis hammer hit locations.**

Over multiple days, multiple hammer hits were recorded at each grid location. During this testing only one of the two traffic lanes on the bridge was shut down. With this traffic present during testing, an effort was made to record hammer hits at times when other vehicles were not on the bridge.

One hammer impact is presented in figure 7. This impact occurred at location 2B and was sampled at 1000 Hz. The bridge's acceleration response to this impact is presented in figure 8. In the zoomed-in view, the downward acceleration of the sensor directly below the hammer hit is clearly seen.



**Figure 7. Graphs. Hammer impact at location 2B.**



**Figure 8. Graphs. Acceleration response of all accelerometers to hammer impact at location 2B.**

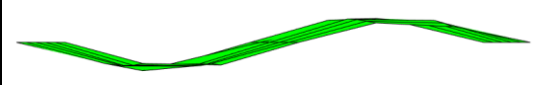

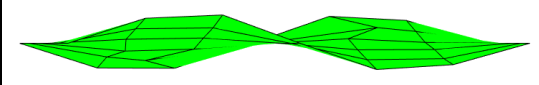
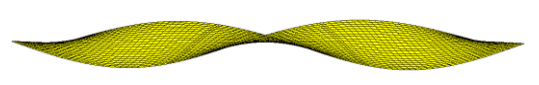
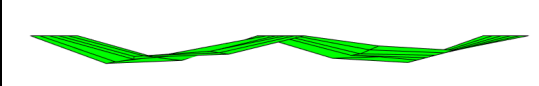

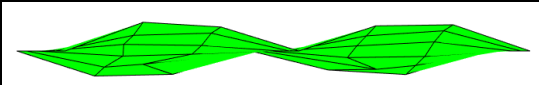

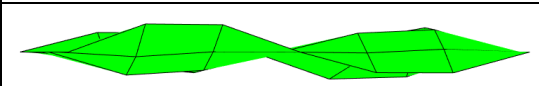
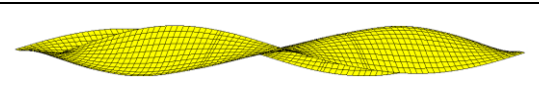
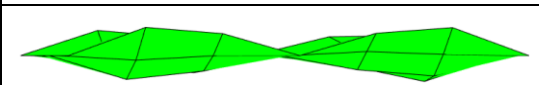
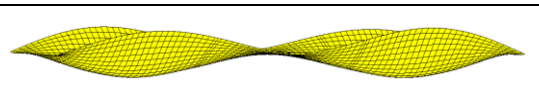
### Modal Analysis

Both the eigensystem realization algorithm (ERA) and the numerical algorithms for subspace state space system identification (N4SID) are selected to perform the modal analysis.<sup>[3, 4]</sup> Both methods utilize the excitation input and the structure's output to determine the structure's modal properties, which include natural frequencies, damping ratios, and mode shapes. Both ERA and N4SID were used to analyze the separate hammer hits collected at the locations shown in figure 6. The results from each test were averaged together, after first removing outliers and are shown in table 1. The mode shapes from different tests were also averaged together, after first discarding any inconsistent mode shapes. The mode shapes are presented in table 2, alongside the mode shapes from an initial finite element model of the bridge.

**Table 1. Modal analysis results.**

Mode	Frequency (Hz)	Damping Ratio (%)
1	3.61	0.46
2	4.19	0.61
3	5.33	2.43
4	5.73	1.66
5	6.65	0.96
6	7.45	0.82

**Table 2. Mode shape comparison between experimental modal analysis results and the initial FE model.**

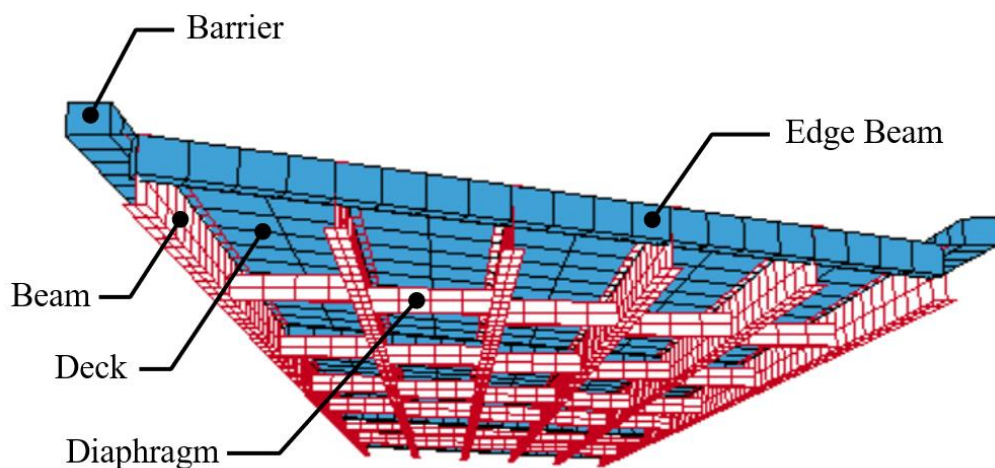
Mode	Experimental	FE Model
1		
2		
3		
4		
5		
6		

## FINITE ELEMENT BRIDGE MODELING

A finite element (FE) model of the bridge has been created in LS-DYNA. This program excels in performing dynamic finite element simulations. This section explains the details of the model and how it is updated to match the as-built bridge.

### Finite Element Model Creation

The FE model was created using the original bridge construction drawings. The FE model is shown in figure 9, which is a view of the underside of the bridge. The concrete deck is modeled with four node quadrilateral shell elements. The deck is subdivided so the length of each shell is approximately 50 inches. The shell material properties are defined to match those of 4,000 psi (Class AA) concrete. The bridge beams are modeled with linear beam elements that are typically 25 inches long. At the ends of the bridge, the beams consist of W36×150 sections; at the middle portion of the bridge over Bent 3, the beams are W36×160 sections. The beam material is A572 Grade 50 steel. The diaphragms that are spaced between the beams are modeled with beam elements as well. They consist of MC18×42.7 sections made of A36 steel.



**Figure 9. Diagram. Finite element model of the bridge.**

The middle two spans of the bridge deck were poured with three separate pours. The first pour was in the first two thirds of Span 2, the second pour was in the last two thirds of Span 3, and the third pour was in the last third of Span 2 and the first third of Span 3, which is the negative moment region in the deck. On each side of the construction joints, a 12-inch-wide and 20-inch-thick edge beam was poured. Edge beams of the same dimension were also poured at the beginning of Span 2 and the end of Span 3, where the expansion joints are. These edge beams are modeled with shell elements with the same concrete material as the deck. The final bridge component modeled was the concrete barriers on top of the deck. These are modeled as rectangular beam elements with concrete material properties.

### **Comparison of Finite Element Model and As-Built Bridge**

With the FE model built, the LS-DYNA eigenvalue solver can be utilized to determine the dynamic properties of the model. A comparison of the first six mode shapes from the experimental modal analysis and the FE model is presented in table 2. From the comparison, the mode shapes visually match well, indicating the first six modes from the FE model correspond to the first six modes from the experimental modal analysis. This observation is confirmed by the modal assurance criterion (MAC). The MAC value is a scalar number that indicates how similar two vectors are, with a MAC value of one indicating that the vectors are identical and zero indicating that they are orthogonal. The MAC values comparing the FE model mode shapes to the experimental mode shapes are included in table 3. All MAC values are relatively close to one, which confirms that mode shapes from the FE model match well the experimental mode shapes.

Table 3 also presents a comparison of the experimental and FE model natural frequencies. The FE model frequencies for modes one and three are lower than experimentally observed, while

modes two, four, five, and six have FE model frequencies higher than experimentally observed. To make the FE model better represent the actual structure, finite element model updating is needed.

**Table 3. Comparison of natural frequencies for the first six modes.**

Mode	MAC Value	Natural Frequency (Hz)	
		Experimental	FE Model
1	0.9946	3.61	3.45
2	0.9654	4.19	4.62
3	0.9401	5.33	5.23
4	0.9722	5.73	6.36
5	0.9687	6.65	8.83
6	0.9581	7.45	9.62

## Finite Element Model Updating

### *Model Updating Background*

From the FE model, modal properties can be extracted and compared to the experimental modal properties obtained from the hammer testing. Differences between the modal properties indicate that the FE model does not represent the true structure as well it could. FE model updating is the process used to change model parameters to make the model more closely match the as-built structure.

The modal properties depend on the mass, stiffness, and damping properties of the model. It is often reasonable to assume that the mass of the structure is decently modeled, since the structure dimensions and material densities tend to not vary greatly. Greater variation in the stiffness-related parameters in the model, however, is expected. One such parameter is the elastic modulus

of the concrete. This is related to the compressive strength of the concrete, which is typically provided higher than specified on the construction plans. This results in the poured concrete being stiffer than the nominal value. Moreover, considering day-to-day operational variability, it has been found that the elastic modulus of concrete changes more significantly with temperature changes than it does for steel.<sup>[5]</sup> Another parameter with variability is the stiffness of the bridge supports. Initially, in the FE model the supports are considered ideal, with the fixed directions fully restrained and the free directions fully released. In reality, some finite stiffness for these supports can be optimized via model updating. Regarding damping, the damping levels observed for bridges are relatively low and assumptions such as Rayleigh damping may be sufficient.<sup>[6]</sup> If nonproportional damping is observed, it may be appropriate to update damping parameters; however, that is not considered in this research.

The model updating was performed for this research via SMU, a Structural Model Updating software package hosted publicly on GitHub.<sup>[7]</sup> SMU runs in MATLAB and utilizes the optimization algorithms provided with the MATLAB optimization toolbox.<sup>[8]</sup> SMU requires as inputs the stiffness and mass matrices from the FE model, along with the stiffness influence matrices that indicate how the updating variables affect the stiffness matrix.

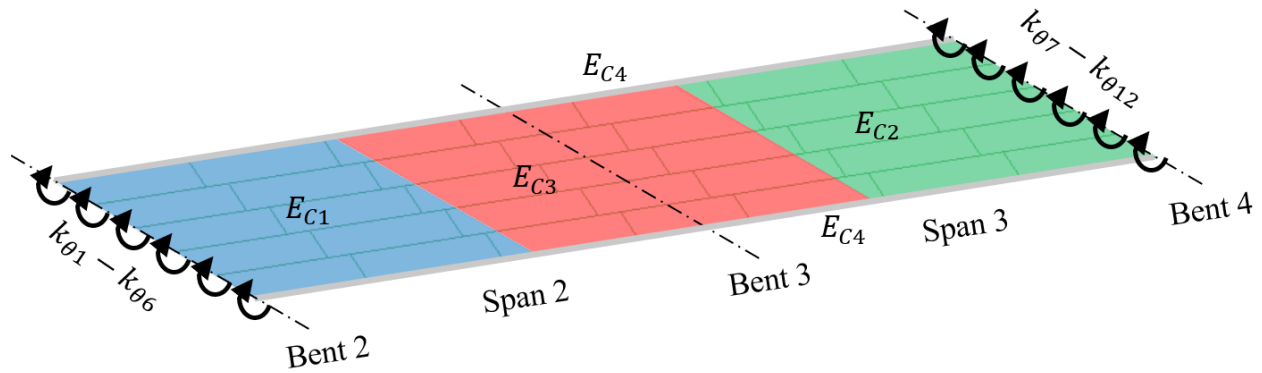
SMU offers three different model updating formulations. The first is the modal property difference with a MAC (modal assurance criterion) values approach. This formulation seeks to minimize the differences between the measured and FE model natural frequencies, and it seeks to minimize the differences between the measured and FE model mode shapes by way of the MAC value criterion. The second updating formulation implemented in SMU is the modal property difference with an eigenvector difference approach. This approach is similar to the first formulation, but instead of optimizing MAC values, the magnitude of the difference between the



measured and FE model mode shapes (eigenvectors) is minimized. The third formulation is the modal dynamic residual formulation. This formulation seeks to minimize the residual of the generalized eigenvalue problem using the measured natural frequencies and mode shapes and the FE model stiffness and mass matrices.

### ***Model Updating Setup***

Some of the parameters selected to be updated for the LaGrange bridge are identified in figure 10. First, there are three concrete elastic moduli selected as updating parameters:  $E_{C1}$  for the concrete used in the first deck pour,  $E_{C2}$  for the second deck pour, and  $E_{C3}$  for the third deck pour. Not shown is a fourth concrete stiffness parameter,  $E_{C4}$  for the concrete parapets. Next, the rotational stiffnesses at the supports at both ends of the bridge— $k_{\theta 1}$  through  $k_{\theta 12}$ —are selected as updating parameters to replace the frictionless bearing assumption. Since the modal properties were obtained only considering vertical motion, the lateral and longitudinal support stiffnesses were not considered as updating variables. Lastly, to account for other modeling uncertainties, such as the final haunch thickness between the beams and the deck, the elastic moduli of the steel beams are added as updating variables. Each beam is divided into three sections: W36x150, W36x160, and W36x160 with top and bottom cover plates. The steel material stiffness for each of the sections for each beam is selected as an updating variable, resulting in 18 additional variables. The total number of updating variables is 34.



**Figure 10. Diagram. Bridge model with updating parameters labeled.**

### ***Model Updating Results***

The model updating was run using the six modes resulting from the modal analysis. Table 4 presents a comparison of the natural frequencies from before and after the model updating. A higher weighting was applied to the first two modes, since they are the more dominant modes that are excited when vehicles cross the bridge. This weighting resulted in good match between the first two experimental and updated model natural frequencies. The third natural frequency was not improved; however, there was less certainty in its experimental value as it did not appear in many of the hammer tests. The fourth through sixth modes also saw improvement.

**Table 4. Comparison of natural frequencies for the updated model.**

Mode	Natural Frequency (Hz)		
	Experimental	Original Model	Updated Model
1	3.61	3.48	3.60
2	4.19	4.65	4.20
3	5.33	5.29	5.22
4	5.73	6.43	5.69
5	6.65	8.85	7.65
6	7.45	9.67	8.43

## **CHAPTER 2. CONTROLLED BWIM FIELD TESTING**

This chapter presents the BWIM validation that was performed using a loaded truck with known wheel weights. Following an introduction, the details of the control truck are provided. Next, the test details and collected data are presented. Then, the sensors used for truck detection during the testing are described. Finally, the BWIM analysis is presented, which includes a description of the BWIM algorithm used, along with the BWIM results.

### **INTRODUCTION**

A controlled BWIM test was performed on June 16, 2021, using a loaded Georgia Department of Transportation (GDOT) dump truck with known wheel weights. The purpose of this testing is to validate the installed instrumentation and test the accuracy of the BWIM algorithm. Additionally, the control testing allows for the tuning of the BWIM algorithm parameters.

To perform the testing, one lane of I-85 over the bridge was closed. The testing consisted of both static and dynamic tests. For the static tests, the truck drove to specific locations on the bridge and stopped for a period. For the dynamic tests, the truck drove across the bridge at specified speeds. Both GoPro videos and time-lapse cameras were utilized to document the tests. These resources are useful for verifying test information such as truck position and timing.

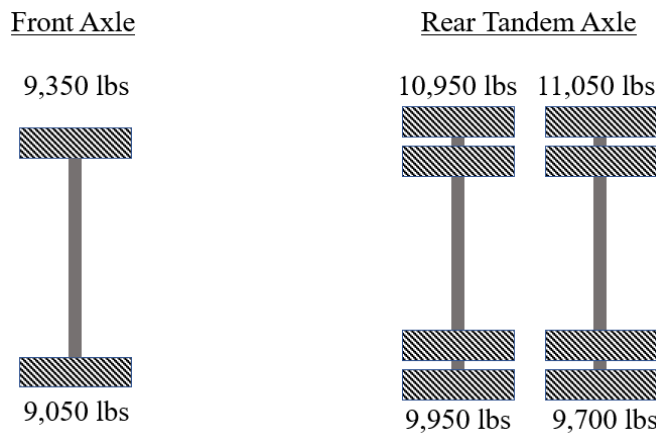
### **CONTROL TRUCK DETAILS**

The truck used for the control tests is a GDOT tandem-axle dump truck and is shown in figure 11. The truck has a single front axle and a tandem rear axle. The truck was loaded during the testing and had a gross vehicle weight (GVW) of 60,050 lb. The weight of the truck was determined

using a portable scale with an accuracy of  $\pm 50$  lb. The weight breakdown by axle and wheel group is shown in figure 12.



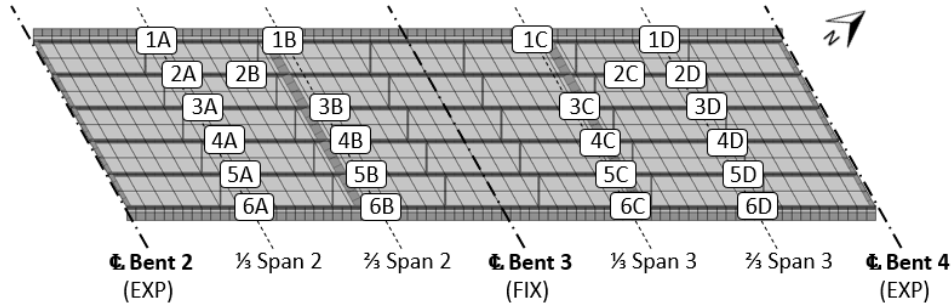
**Figure 11. Photo. GDOT dump truck with axle spacings dimensioned.**



**Figure 12. Diagram. Dump truck wheel weights.**

## TEST DETAILS AND DATA

This section presents a selection of the data collected from both the static and dynamic tests. For all plots, the sensor locations are matched to the sensor group names defined in figure 13. The labels have two parts: the first is a number (1 through 6) that corresponds to the beam number, and the second is a letter (A through D) that identifies the position along the beam.



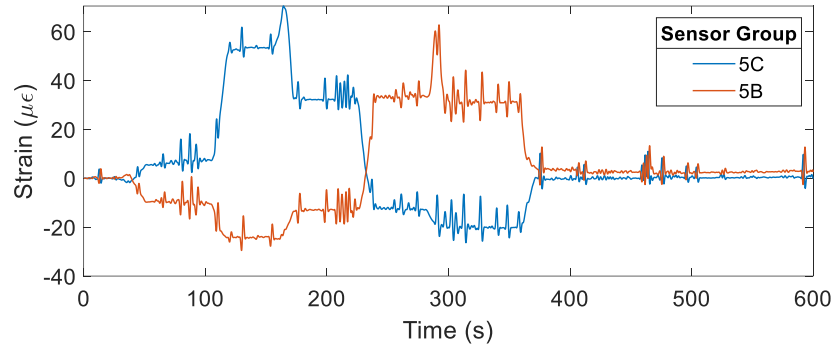
**Figure 13. Diagram. Sensor group labels.**

### Static Tests

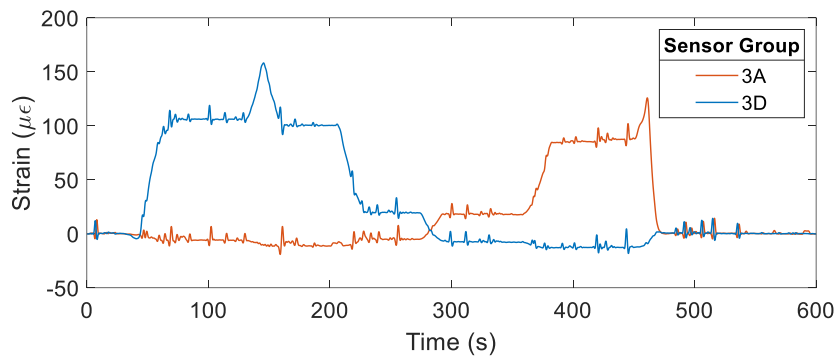
Two static tests were completed: one with the truck in the left lane and one with the truck in the right lane. The purpose of these tests was to determine the static response of the strain gages to a known loading. These measurements can be used for validating the FE model and validating that the sensors are working correctly. For example, an improperly installed strain gage can be identified from the test data. Additionally, the tests can be used to obtain experimental strain influence lines, which may be beneficial for the BWIM accuracy. For both tests, the truck stopped at five locations on the deck for at least 30 seconds so that the bridge response minus any dynamic effects could be measured. The sensors were sampled at the relatively low rate of 10 Hz for these tests. Since the dynamic response of the bridge was not of importance for these tests, no acceleration data were collected.

Data from select strain gages are presented in figure 14 and figure 15. Each figure plots the response of one strain gage in Span 2 and another in Span 3. The data presented have been post-processed with a low-pass filter. This was necessary because while the truck was mostly stationary during the tests, there was traffic crossing in the opposite lane, which added undesired noise to the strain measurements. The first figure is from the static test with the truck in the left lane, and the second figure is from the static test with the truck in the right lane. Both figures

distinctly show how the truck stops at five different locations on the bridge during the test. As expected, when the truck is closer to a strain gage and in the same span, there is a larger positive strain signal measured. When the truck moves to the opposite span, the strain signal becomes negative, corresponding to downward curvature at that sensing location.



**Figure 14. Plots. Left lane static test strain data at select points.**



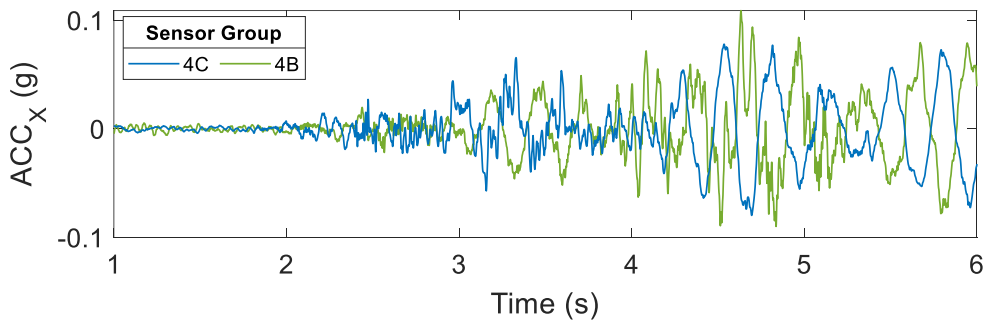
**Figure 15. Plots. Right lane static test strain data at select points.**

### Dynamic Tests

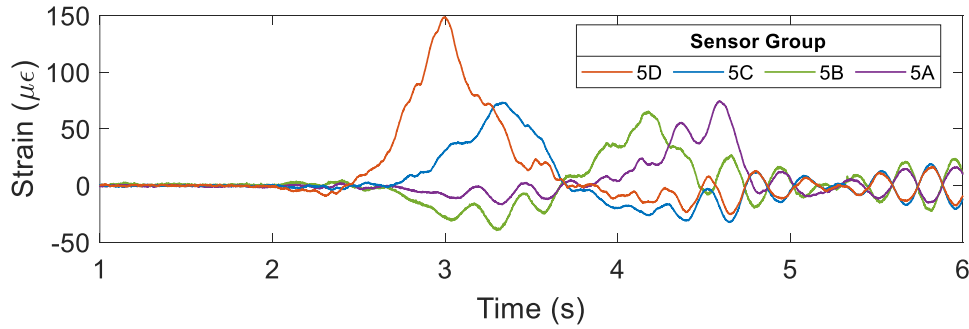
For the dynamic tests, the dump truck crossed the bridge at a constant speed. Tests were performed with the truck driving in either the left or right lane. One lane of traffic was always shut down during the tests, which helped to ensure that while the truck was crossing it was the

only vehicle on the bridge. For all dynamic tests, the sensors were sampled at 1000 Hz for 12 seconds. The dynamic testing started at 10:30 AM and concluded at 1:00 PM.

Examples of the data collected are shown in figure 16 and figure 17. These figures plot the bridge response at select sensors using data from one test run, where the truck traveled in the left lane at 50 mph. Acceleration data are plotted in figure 16. The presence of the truck is slightly visible in the acceleration signal around 3 seconds in, but what is more obvious is that the truck causes the bridge to vibrate with increasing magnitude as it passes over. Strain gage data are plotted in figure 17. The path the truck travels can be seen by following the peaks in the figure. First, the truck crosses over the strain gage at sensor group 5D, then 5C, 5B, and 5A, respectively. When the truck is over the sensors it creates positive bending, and when it is in the other span it leads to negative bending, as expected. Also, the low-frequency bridge vibrations can be seen in the strain signals.



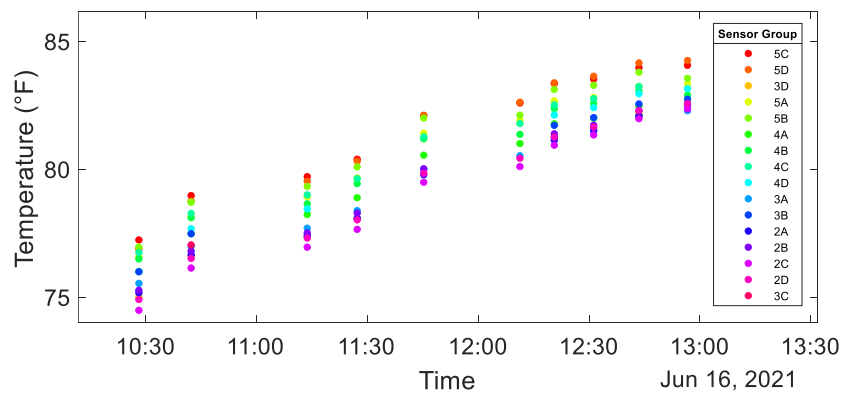
**Figure 16. Plots. Vertical acceleration at select locations.**



**Figure 17. Plots. Bending strain at select locations.**

### Temperature Data

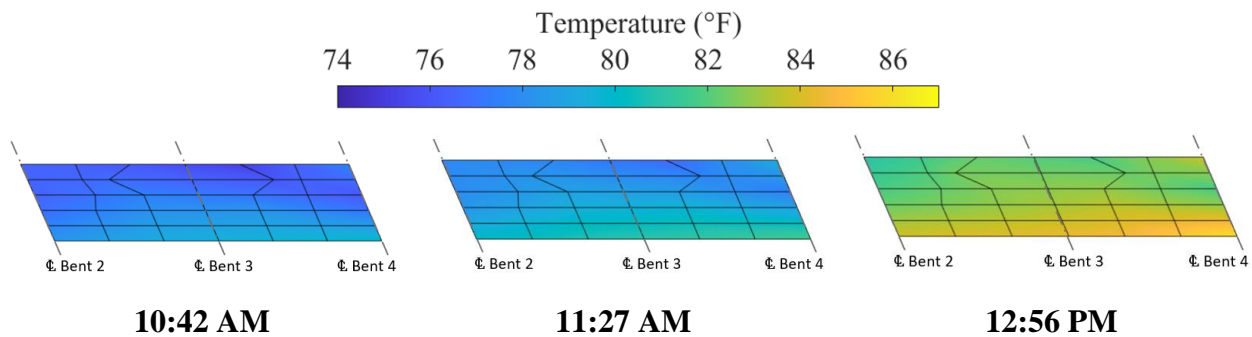
Temperature data were collected for all dynamic tests using the thermistors located next to the strain gages at all interior beam sensor groups. Figure 18 plots the temperature data collected on June 16, 2021, from around 10:30 AM until 1:00 PM. The color of the points corresponds to a sensor group, which indicates the thermistor location. The weather that day was sunny with clear skies. This resulted in the bridge heating up throughout the morning as the sun is rising higher. As the sun approaches its peak, the temperature increase slows down. Also, at this point the entire bridge is trending toward a more uniform temperature than earlier in the morning, i.e., the difference between the maximum temperature and the minimum temperature is decreasing.



**Figure 18. Plots. Temperature over a few hours at interior beam sensor groups.**



Figure 19 pairs the temperature data with sensor locations and the bridge geometry to show the spatial distribution of the temperature at three times on June 16. This plot reveals that at these times of day one side of the bridge is generally hotter than the other. For the times shown, the southeastern facing side of the bridge is hotter, which is logical since the sun would be rising from that direction. Differential heating like this is expected to change the modal properties throughout the day. Ultimately, research needs to be performed to develop a method to utilize temperature information to dynamically adjust the FE model for variable environmental conditions.



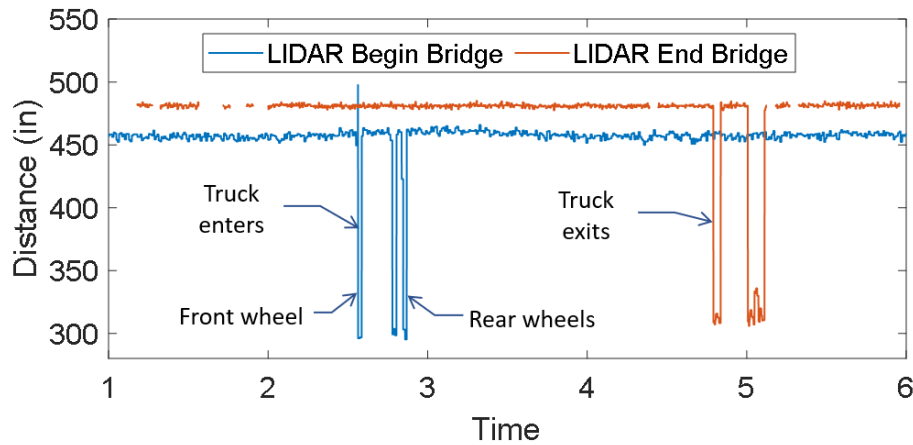
**Figure 19. Plots. Surface plot depictions of beam temperature at different times on June 16, 2021.**

## TRUCK DETECTION WITH LIDAR

For the dynamic testing there were two distance sensors added on top of the bridge deck to detect the truck location and speed. These sensors were Garmin LIDAR-Lite v3HP devices interfaced with *Martlets*. These one-dimensional LIDAR (light detection and ranging) devices measure the distance to an object by timing the duration it takes for a laser to reflect off the object. The devices used have a range of up to 131 ft and can take measurements at a rate of 1 kHz with an accuracy of  $\pm 1$  inch. The devices were placed at the beginning and end of the bridge and were

positioned at ground level perpendicular to the direction of travel so that the distance to the wheels of the truck would be measured.

The measured LIDAR signals from the test are plotted in figure 20. In the figure, the first LIDAR sensor detects the front wheel and then the two subsequent wheels as they pass by the sensor. The front wheel is detected by the LIDAR sensor at the end of the bridge 2.227 seconds later. The distance between the two sensors is 159.45 ft; therefore, the speed of the truck is calculated to be 48.8 mph. The intended speed of the truck for this test was 50 mph, so the LIDAR measurements appear to be accurate. Additionally, the distance from the gutter line to the wheels is measured to be around 300 inches or 25 ft, correctly indicating that the truck was traveling in the left lane while entering and exiting the bridge.



**Figure 20. Plots. Detection of truck wheels with LIDAR sensors.**

## **TRUCK DETECTION WITH DECK-MOUNTED STRAIN TRANSDUCERS**

An alternate—and more experimental—approach to detecting trucks is to use strain transducers mounted to the underside of the concrete bridge deck. Strain transducers are utilized in this application for their mounting ease and durability compared to metal foil strain gages, which are

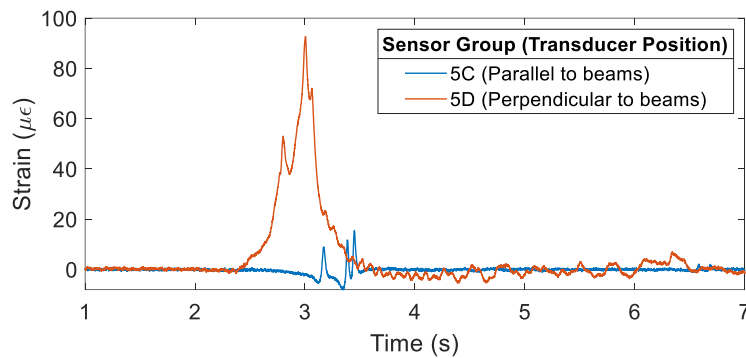
more challenging to directly mount on concrete. The concept of this truck detection approach is that when a vehicle wheel passes over the strain transducer, a peak in the measured strain signal should be notable. If two strain transducers are placed along the lane of travel, then the time between peaks and the distance between the transducers can be used to calculate the vehicle speed. Since each axle creates a peak, the vehicle speed can be used to estimate the axle spacings.

Four strain transducers were installed on the underside of the deck, and their locations are shown in figure 4. Two strain transducers are located underneath the right lane in Bay 4 (between Beams 4 and 5), and the other two are located underneath the left lane in Bay 5 (between Beams 5 and 6). The optimal orientation of the transducers for axle detection was unknown, thus in each bay one transducer is placed parallel to the beams and the other is placed perpendicular to the beams. The strain transducers are interfaced with the *Martlets* that were closest to their location. These *Martlets* therefore each collect data from the following four channels: vertical acceleration, deck transducer strain, beam bending strain, and temperature.

The left-lane strain transducer signals from the test are plotted in figure 21. When crossing the bridge, the truck first passes over sensor group 5D and then 5C. The first notable observation from the data is that the magnitude of the deck strain is much higher in the direction perpendicular to the beams. For each transducer, three peaks can be seen, corresponding to the front axle and rear tandem axle. However, for the transducer parallel to the beams, the peaks are much more distinct. This trend is observed over multiple tests. Therefore, a recommendation for a future implementation is to place all strain transducers parallel to the beams.

From the offset in the transducer signal peaks, the speed of the truck is estimated to be 49.1 mph, which is just 0.3 mph more than the LIDAR estimate. With the performance of the deck-

mounted strain transducers being comparable to the LIDAR sensors, it is recommended to focus on strain transducers for future BWIM implementations. The LIDAR sensors require additional *Martlets* and solar panels, and they are more susceptible to environmental damage. For a long-term installation, the durability and reliability of the strain transducers is expected to result in them outperforming the LIDAR sensors.



**Figure 21. Plots. Detection of truck wheels with strain transducers.**

## BWIM ANALYSIS

With an accurate bridge model created and response data collected from crossing trucks, the BWIM analysis can be performed to estimate axle weights. In general, the axle weights are determined by comparing the expected response of the bridge to the measured response, using the estimated axle positions at each time instant. The details of how this is accomplished are dependent on the BWIM algorithm selected.

## BWIM Algorithms

The algorithms that have been proposed to perform BWIM fall into two categories: influence line algorithms and moving force identification (MFI) algorithms. The algorithms that are based on influence lines are usually a variation of the first BWIM algorithm proposed by Moses.<sup>[9]</sup> The basic concept of this method is that a bridge's strain or displacement response to a truck can be

compared to a predetermined influence line to determine the weight of the truck. While these algorithms have had success, they essentially treat the BWIM problem as a static one and find different ways to reduce the dynamic effects present in the measurements.<sup>[10]</sup> MFI algorithms attempt to provide improved BWIM accuracy by directly modeling the bridge dynamics.<sup>[11-13]</sup>

The BWIM problem can be viewed as falling into the more general input force estimation problem in structural dynamics. Input estimators seek to use the measured response of a structure to inversely determine the input force that acted on the structure. There are only a few published attempts at using input estimators for BWIM.<sup>[14-16]</sup>

To perform BWIM for this research, a recently developed input estimation algorithm, called the finite input covariance (FIC) estimator is adopted.<sup>[17]</sup> The FIC estimator works recursively, providing a new estimation of the input every time a new measurement is available. The estimator is founded on the assumption that the input is a zero-mean Gaussian random variable with finite covariance. This means that each input estimate is independent of the previous estimates. Since the covariance is finite, a value must be assumed, which can be done through either tuning or using prior knowledge of the input variability.

### **BWIM Results – Simulation**

Before the instrumentation plan was finalized, simulations were run with different sensor layouts to determine the optimal number and locations of the sensors. Presented here are the results from three different layouts. For the first layout, the sensors are located at the beam quarter points, which results in 36 different sensor groups, i.e., 36 *Martlets* installed on the bridge. The second layout places the sensors at the beam third points, which results in 24 sensor groups. The third layout places the sensors at the beam half points. As this results in one sensor per span per beam,

strain gages measuring the negative bending over Bent 3 are included in this layout for each beam, resulting in 18 sensor groups for this layout.

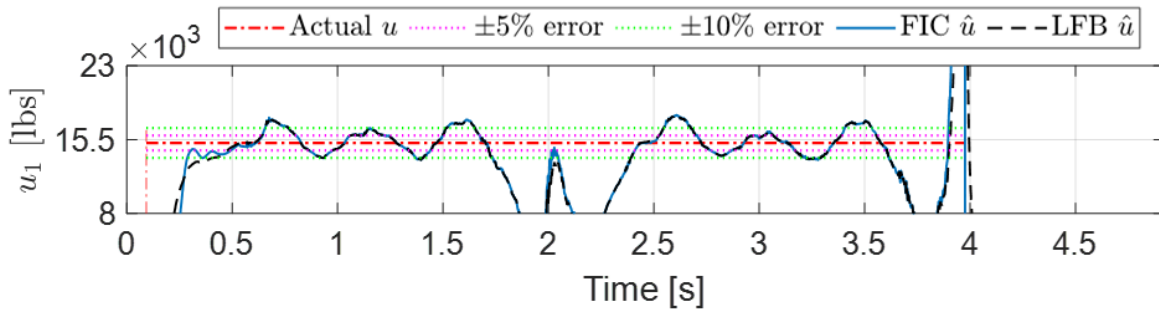
The simulations are run in LS-DYNA using a loading pattern that closely resembles the control testing truck. The simulation truck has a front axle weighing 15,150 lb and a tandem axle weighing 21,300 lb. The GVW is therefore 36,450 lb. The truck wheel loads are modeled as simple spring-mass-damper point loads. The deck of the bridge is set as a contact surface, and the wheels are defined so that they do not penetrate the deck. A constant velocity is assigned to the simulated truck. An explicit analysis is run, and simulated sensor data are extracted from the output. These sensor data are then fed to the BWIM algorithms. For the simulations, the results of the FIC estimator are compared to results using a limited frequency bandwidth (LFB) estimator. The LFB estimator is an extension of the FIC estimator that includes a model of the input. This can provide more accurate results when input details are known in advance, such as the frequency bandwidth of the excitation.

The BWIM results from the simulations are presented in figure 22, figure 23, and figure 24. All three figures include a plot of the weight estimation for the front axle, denoted  $u_1$ ; a plot of the weight estimation for the rear tandem axle, denoted  $u_{2,3}$ ; and a plot of the weight estimation for the gross vehicle weight, denoted  $u_t$ . Each plot includes lines that indicate the true weight, denoted  $u$ , as well as lines indicating the 5 and 10 percent error range. Figure 22 contains the results from the layout with the sensors located at the span quarter points. Figure 23 contains the results from the layout with the sensors located at the span third points. Lastly, figure 24 contains the results from the layout with the sensors located at the span half points.

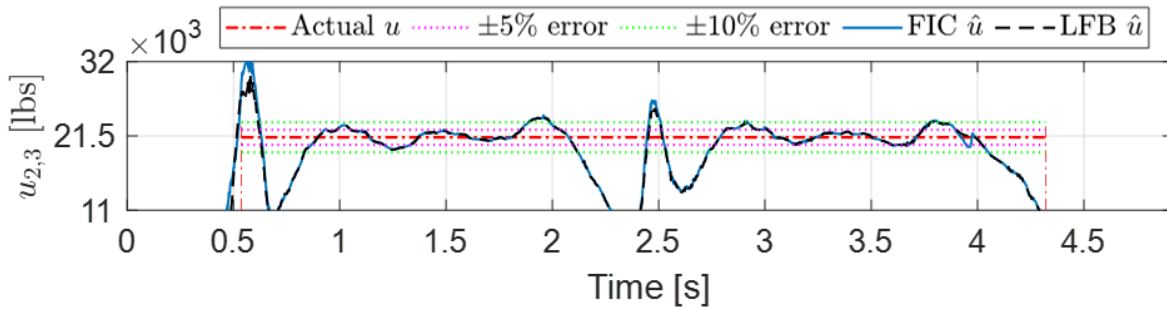
These figures show that the weight estimation is most accurate when the truck is located near the middle of Span 2 or Span 3. This accuracy is likely due to the larger strain signals at those instances and due to the larger direct feedthrough of the input to the accelerometers when the truck is directly over them. When the truck is at the beginning or ends of a span, the weight estimates are poor, which is due to the truck being over or near a bent at those times. Comparing one figure to another, as the number of sensors on the bridge decreases, the weight estimation becomes less stable.

The BWIM algorithms provide a time history of the weight estimates; however, to compare to the actual weight or weight limits, a single estimate for each axle is needed. This estimate is obtained by averaging the weight estimates only at times when the axle is in the middle third of the span, i.e., between sensors. This results in the poor estimates at the ends of the spans being ignored.

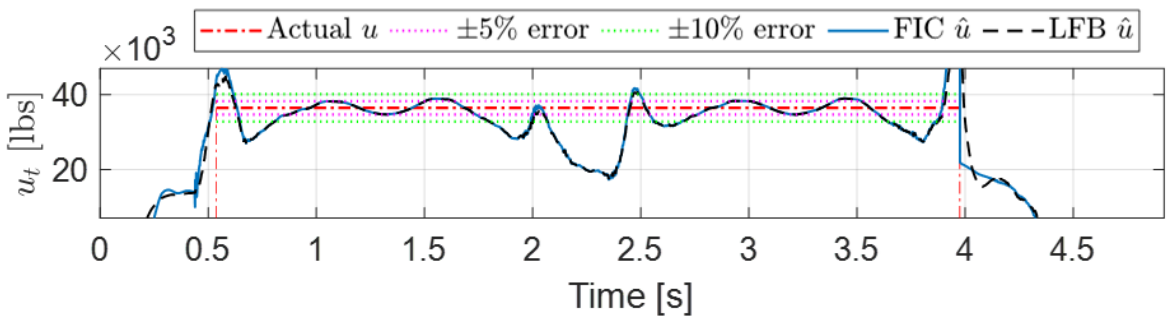
Table 5 presents the estimation error for the FIC estimates for the three sensor layouts. The results indicate that all three layouts provide decent accuracy, with the sensors at the quarter-point layout performing the best. Of interest is that the sensors at the half-point layout outperform the third-point layout for GVW estimation. This may be due to the addition of the negative moment region strain gages at Bent 3.



**A. Estimation of front axle load,  $u_1$ .**



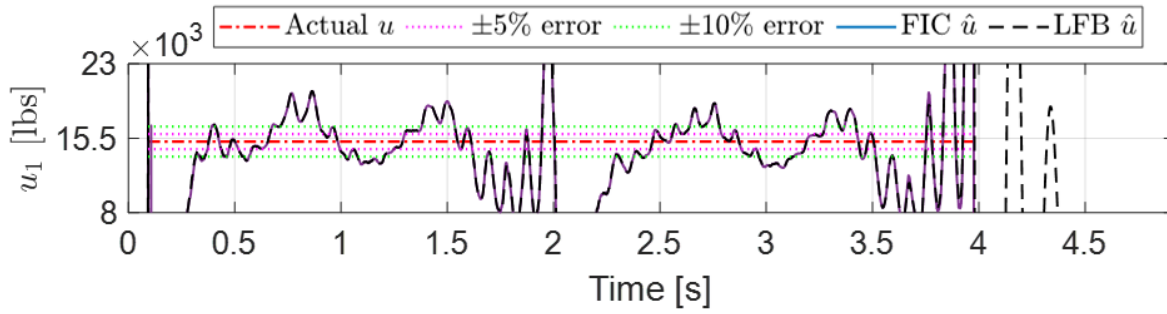
**B. Estimation of tandem axle load,  $u_{2,3}$ .**



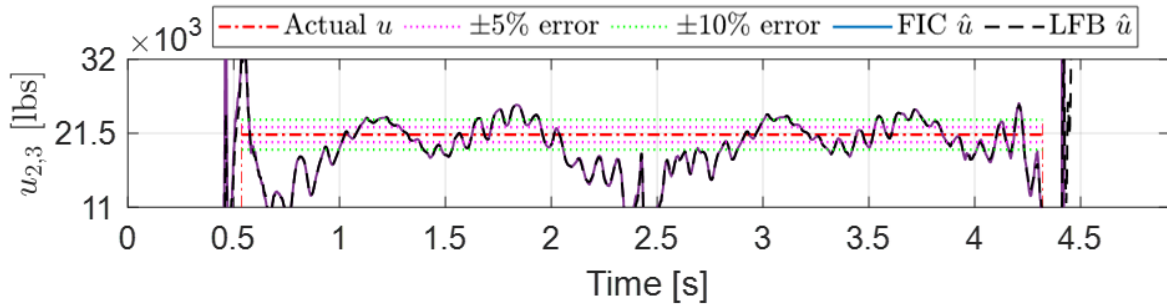
**C. Estimation of GVW,  $u_t = u_1 + u_{2,3}$ .**

**Figure 22. Plots. BWIM simulation results for sensors at beam quarter points.**

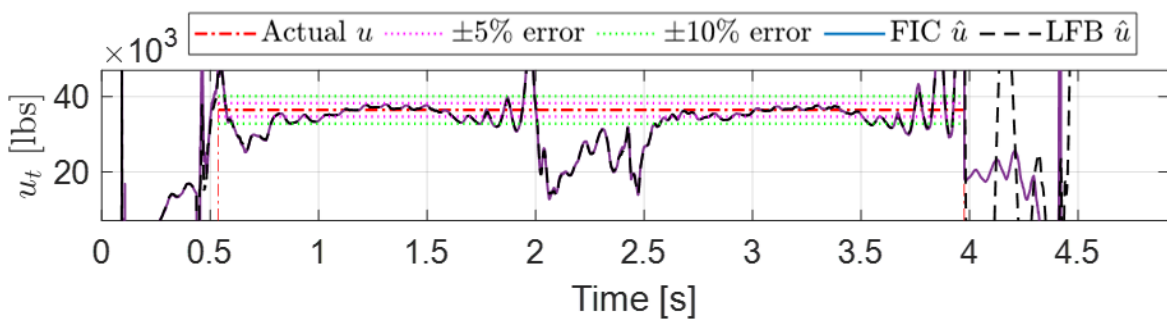




**A. Estimation of front axle load,  $u_1$ .**

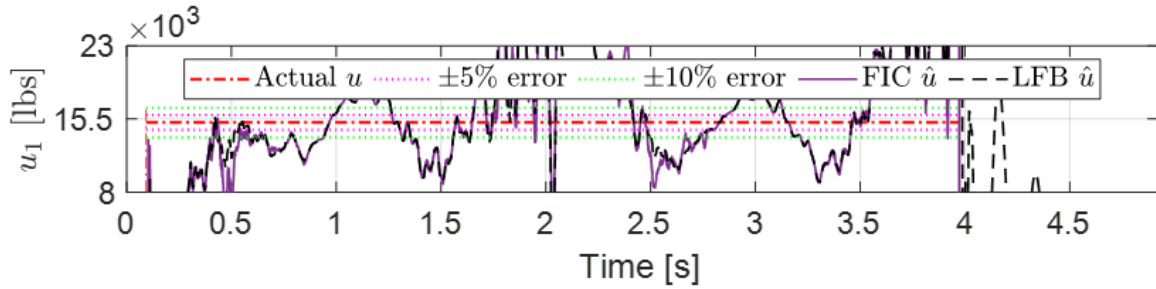


**B. Estimation of tandem axle load,  $u_2 + u_3$ .**

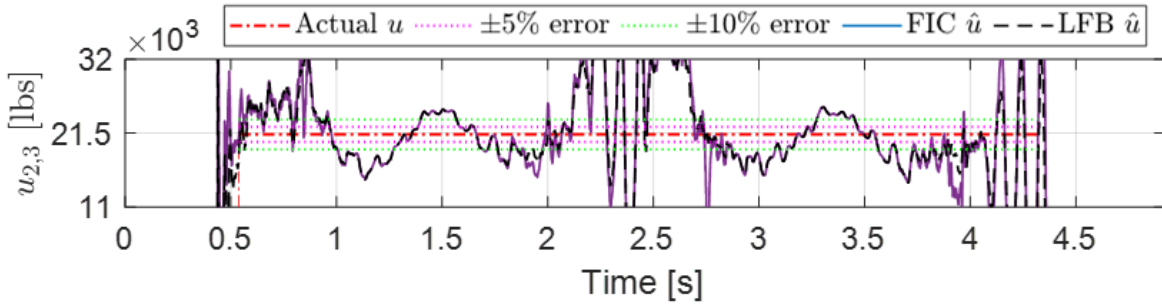


**C. Estimation of GVW,  $u_t = u_1 + u_2 + u_3$ .**

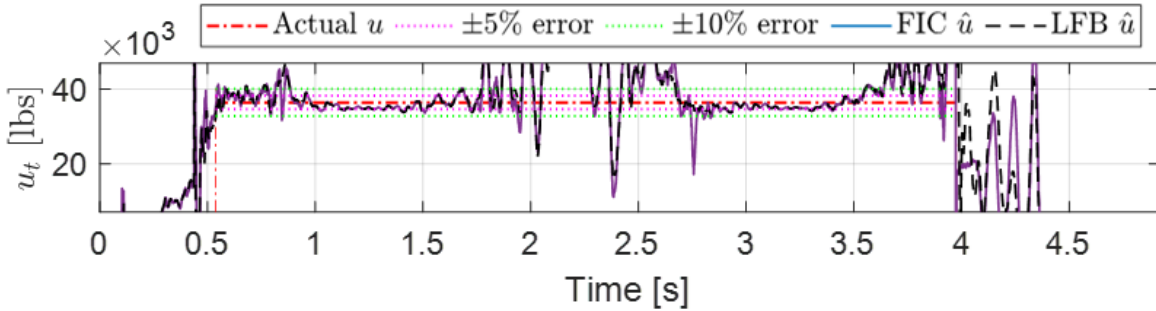
**Figure 23. Plots. BWIM simulation results for sensors at beam third points.**



**A. Estimation of front axle load,  $u_1$ .**



**B. Estimation of tandem axle load,  $u_2 + u_3$ .**



**C. Estimation of GVW,  $u_t = u_1 + u_2 + u_3$ .**

**Figure 24. Plots. BWIM simulation results for sensors at beam half points.**

**Table 5. BWIM simulation estimation results using the FIC estimator.**

<b>Sensor Layout</b>	<b>Front Axle Error (%)</b>	<b>Tandem Axle Error (%)</b>	<b>GVW Error (%)</b>
Quarter Points	1.57	-2.00	-0.51
Third Points	1.58	-6.04	-2.87
Half Points	-3.10	1.72	-0.29

### **BWIM Results – Field Testing**

BWIM analyses were performed using the updated finite element model. For brevity, gross vehicle weight (GVW) estimates are presented from two of the dynamic tests, named Test A and Test B. For both tests the truck traveled in the right lane at the typical 60 mph speed. Figure 25 shows the GVW estimates for Test A using both the FIC (finite input covariance) and LFB (limited frequency bandwidth) estimators. The two subfigures are plotted for two time periods, i.e. when the truck is in the middle of Span 2 and when the truck is in the middle of Span 3. Similarly, figure 26 shows the GVW estimates for Test B over two time periods and using two estimators. For each test and each estimator, average value of the GVW estimates is calculated over the plotted time periods. The percentage errors of these average GVW estimates are presented in table 6. All errors are within 10% and some within 5%.

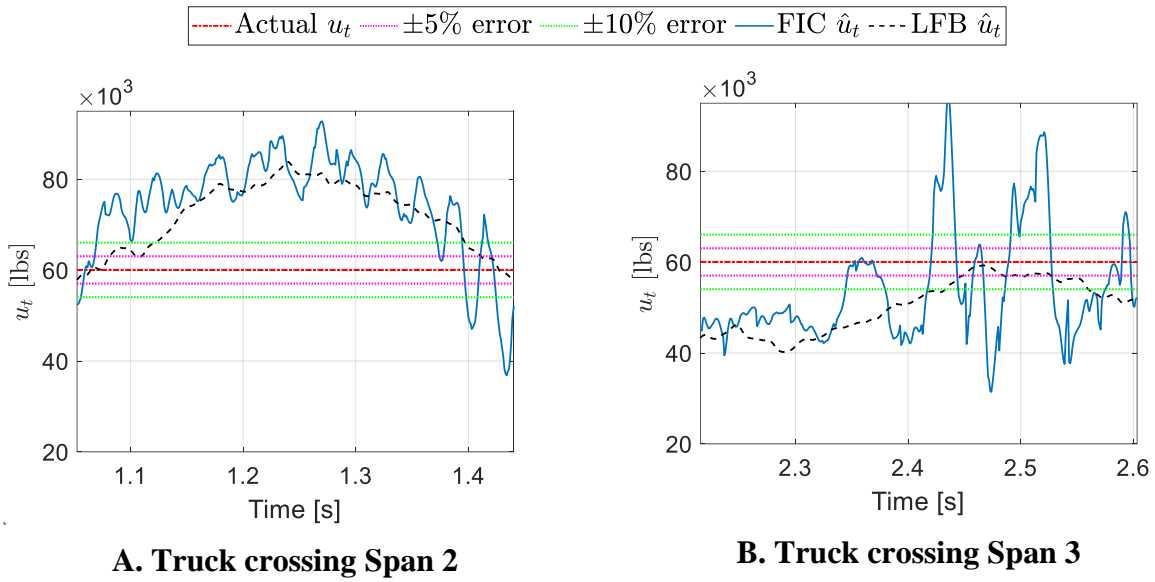


Figure 25. Plots. BWIM GVW estimation results for Test A.

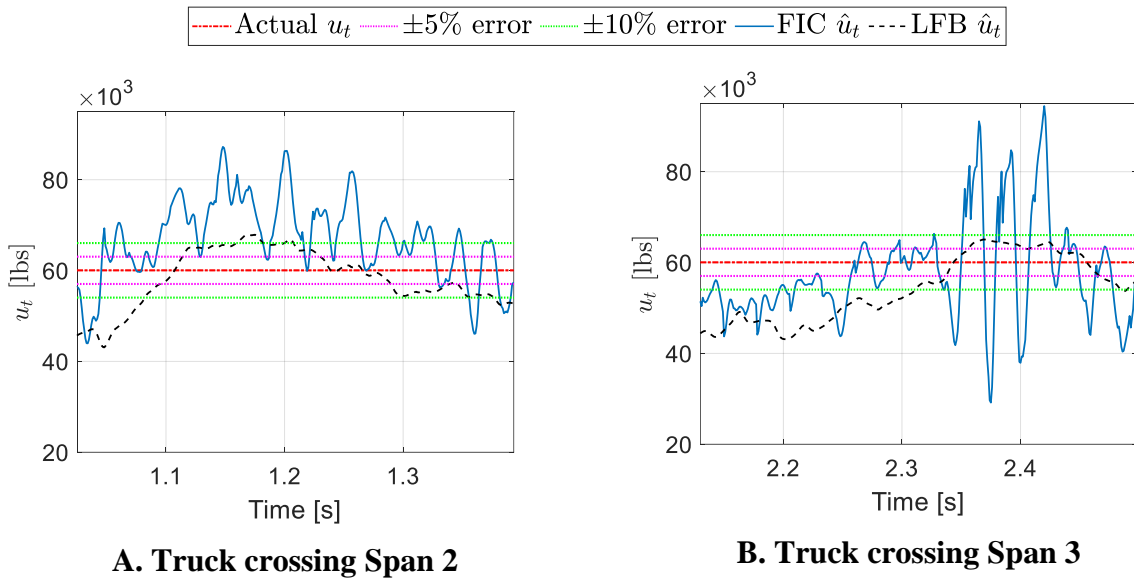


Figure 26. Plots. BWIM GVW estimation results for Test B.

**Table 6. BWIM results from the experimental field test data.**

<b>Test</b>	<b>GVW Error Percentage FIC</b>	<b>GVW Error Percentage LFB</b>
Test A	-4.64%	-7.74
Test B	-1.45	-3.73

## CHAPTER 3. WIRELESS BWIM SYSTEM FIELD DEPLOYMENT

This chapter presents the continuous deployment of the BWIM system. In this chapter, the system is introduced, the system details are described, and then the results from the system implementation are presented. Finally, the findings are summarized.

### INTRODUCTION

The goal of this research was to implement a wireless system that continually performs BWIM at the test bridge. A system to obtain this goal was designed around the *Martlet* platform and was installed at the bridge in September 2021. When designing the system, there were some main technical challenges that needed to be addressed, including how to control the system remotely, how to power the system, and how to detect the presence of trucks. The following section describes how each of these challenges has been addressed.

### SYSTEM DETAILS

A graphic depicting the BWIM system is provided in figure 27. Each of the key components shown in the graphic is discussed in detail in this section. Note that for the continuous field deployment, only 16 *Martlets* remain on Spans 2 and 3, since the accelerometers on the exterior beams were determined to be marginally beneficial for BWIM accuracy.

#### Main Enclosure

A 24×24×6-inch enclosure was installed on the south side of Bent 2. The enclosure, shown in figure 28, has a NEMA Enclosures 3R rating, which means it is suitable for the outdoors and provides protection from rain and ice. Inside the enclosure are the gateway, an Arduino, *Martlets* for solar charging and battery monitoring, and the batteries to power the *Martlets*. Additionally,

there is a four-outlet electrical receptacle that is currently used to provide power to the gateway.

Power wires from solar panels run into the enclosure via a 2-inch conduit, and power wires to the bridge sensors run out of the enclosure via a second 2-inch conduit.

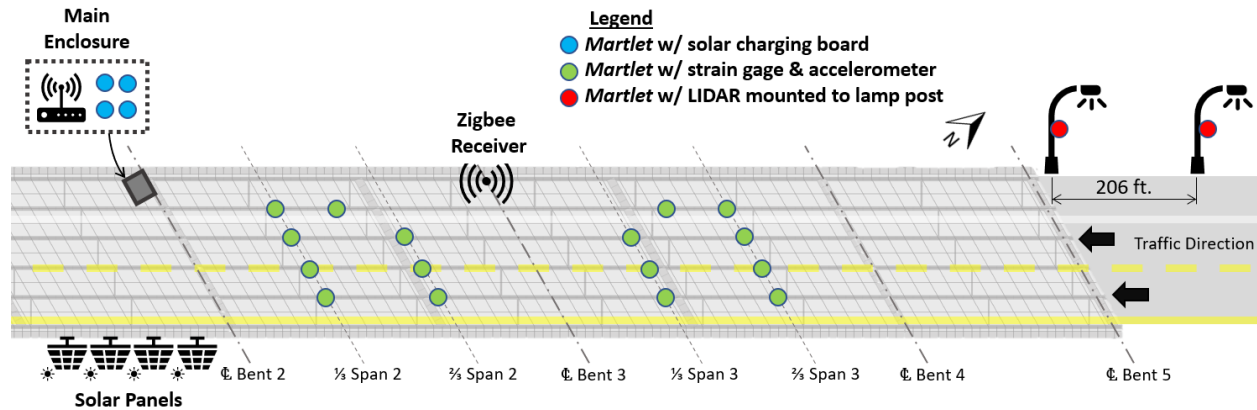
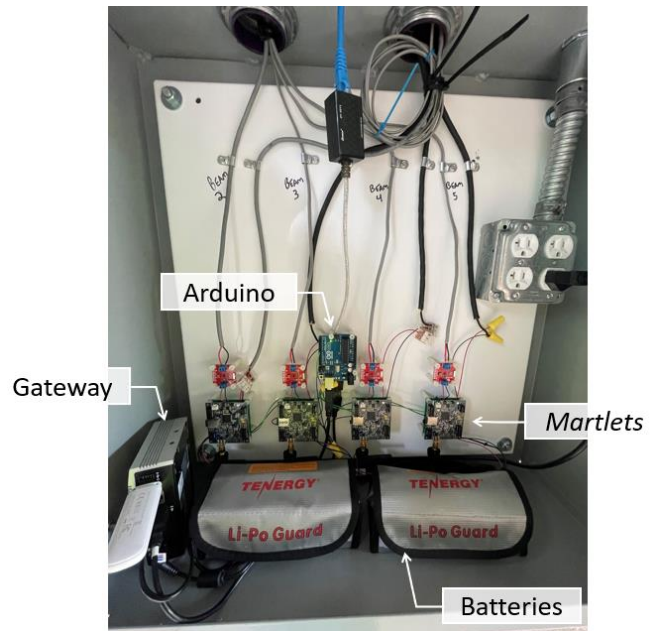


Figure 27. Diagram. BWIM system overview.



A. Outside view



B. Inside view

Figure 28. Photographs. Main enclosure on Bent 2.

## The Gateway

The gateway is located inside the main enclosure. The gateway serves the role of an IoT (Internet of Things) gateway, which is to provide a remote link to communicate with a network of field sensors. The gateway selected for this project is an Advantech ARK-1120 embedded computer. This device has an Intel Atom N455 1.6 GHz processor, 1GB DDR3 memory, and 32GB of CompactFlash memory. Compared to a laptop or desktop, this compact computer sacrifices performance for power savings and at full load consumes just 10.8 watts. Still, it is very capable of running the programs needed to perform BWIM data collection.

The gateway interfaces with the *Martlet* wireless sensors via the *Martlet* signal receiver board. Shown in figure 29, the *Martlet* signal receiver board is inside a small enclosure that is mounted to the north side of Bent 3. The *Martlet* signal receiver is connected to a GPS receiver, and the GPS antenna is magnetically mounted on the steel beam above the receiver. The GPS receiver provides an extremely accurate time signal that is used to synchronize the *Martlet* devices during data collection. The receiver is also connected to a high-gain antenna, shown at the top of figure 29-A, which helps provide a strong wireless link to the *Martlet* devices. The *Martlet* signal receiver is hardwired to the gateway via an ethernet cable.

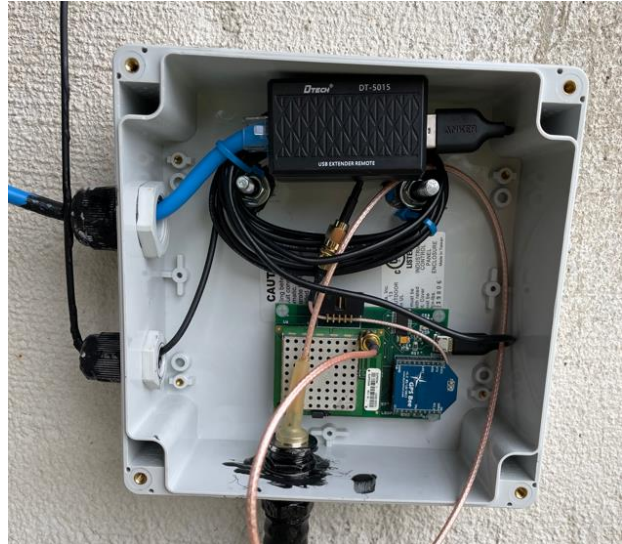
Remote communication is established with the gateway via a 4G LTE modem. The gateway is running VNC® software that allows for a remote desktop connection from another computer or even a smartphone. The VNC connection is primarily for maintenance purposes. For data transmission and storage, Dropbox is utilized. When data from a BWIM test are collected, they are saved to a Dropbox folder and automatically uploaded to the cloud. Periodically the files are



moved to another cloud folder that is not synced to the gateway, which removes them locally from the gateway and frees up memory.



**A. View from below.**



**B. View inside the small enclosure.**

**Figure 29. Photographs. *Martlet* receiver and antenna on Bent 3.**

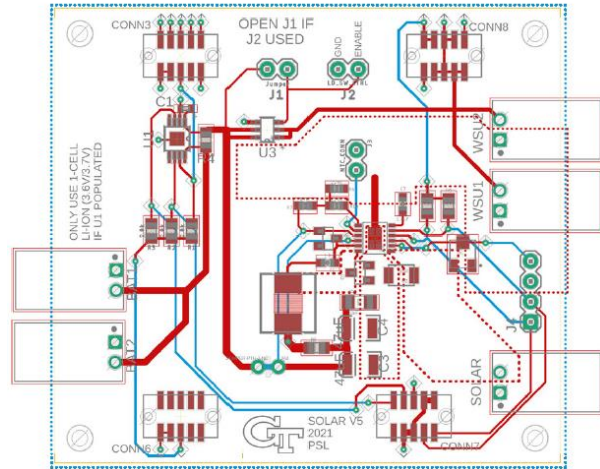
### **Solar Energy Harvesting**

To provide continuous power to the wireless devices, a solar charging system was designed to be interfaced with *Martlet*. The system consists of solar panels, shown in figure 30-A; lithium-ion batteries; and a *Martlet* solar charging daughterboard especially designed for this project, shown in figure 30-B. The solar panels can provide up to 10 watts, which is 1.67 amps at 6 volts. Four solar panels are mounted to the outside of the concrete bridge barrier above Bent 2. The panels are placed on the south-facing side of the bridge, which is the optimal location to harness the most solar power. Each panel is connected to two single-cell lithium-ion batteries that cumulatively can store 20.8 amp-hours of power. Each panel and battery set is connected to five

*Martlet* devices, one to control the charging and four on the bridge with strain gages and accelerometers.



**A. Solar panels mounted to the bridge.**



**B. Solar charging board design.**

**Figure 30. Photo and schematic. Solar energy harvesting components.**

The solar charging daughterboard features an LT3652 charge controller. This chip uses maximum power point tracking (MPPT) to regulate the solar panel voltage to the level that provides maximum power. The LT3652 also has a safety timer to stop charging after a certain time has passed to prevent overcharging the battery. Additionally, a long-lead thermistor is connected to the board and runs to the batteries. The LT3652 monitors the thermistor voltage to determine the battery temperature. Charging will be halted if the battery temperature falls below 32 °F or rises above 104 °F, which are considered unsafe temperature ranges for lithium-ion charging. Another key chip on the solar charging daughterboard is the LTC2941, which features a precision coulomb counter to track the power flowing into and out of the batteries. This chip allows the battery charge levels to be monitored via the *Martlet*, similar to the way a laptop or

smartphone displays battery charge. The LTC2941 has programmable charge alert levels, which can be utilized to shut down the system if the battery charge is getting too low.

### **Power-Saving Features**

If the *Martlet* devices are left running at full power consistently, the batteries will be drained in 1 or 2 days. During an ideal day of sunshine, the batteries may charge around 50 percent of their capacity. This is not sufficient to keep the system running continuously; therefore, power-saving features are incorporated into the *Martlet* software.

Four power-saving configurations are now functional for the *Martlet* system. In STANDBY mode of the *Martlet* microcontroller, the clock to the microcontroller's central processing unit (CPU) and all peripheral modules are shut down. In IDLE, any clocks that are needed will keep running and the device essentially pauses at the IDLE instruction. For this reason, the device consumes more power in IDLE mode, but the wakeup time is shorter than in STANDBY since there is less reinitialization needed upon waking up. Each mode has the option to wake up from either a radio interrupt or the watchdog timer. With the radio as the wakeup source, as soon as a new radio message has been received, it will trigger an interrupt that wakes the microcontroller. This allows for a quick wakeup but leaves the radio always consuming power. With the watchdog timer as the wakeup source, the device is awoken when the timer reaches a set time. If there are no radio messages received in the moment that the device is awake, then it will just go back to sleep until the timer awakens it again. While the device is asleep, the radio is turned off, which saves power but also means it may take multiple attempts for the timing to line up for a message to be correctly received, thus resulting in a longer wakeup time.

Currently, the *Martlet* devices on the bridge are most often in STANDBY mode with the radio as the wake source. Leaving the radio on results in more reliable communication, which is important for quickly starting data acquisition when a truck is approaching the bridge. Once data acquisition starts, the device is placed in fully operational mode; when data acquisition concludes, the device returns to STANDBY mode. The data acquisition triggering system detects trucks far enough in advance for the *Martlet* devices to have sufficient time to wake up and stabilize before a truck reaches the bridge.

These power-saving features help push the battery life of the system to an estimated 3 or 4 days. A concern remains that with multiple rainy days in a row the system will have to temporarily be shut down. Letting the batteries run to empty is ill-advised, as then it would be impossible to determine if the system is functioning at all. To prevent this from occurring, the LTC2941 alert function is utilized to alert the gateway when the batteries reach a low threshold. The gateway then can completely shut off the power supply to the *Martlet* devices via a digitally controlled switch on the solar charging daughterboard. With the switch in the open position the current draw from the batteries is reduced to less than 100  $\mu\text{A}$  and solar charging of the batteries can still occur. Once the batteries reach a sufficient charge level, the power supply to the *Martlet* devices is reestablished and the system resumes collecting BWIM data.

### **Data Acquisition Triggering via LIDAR**

Because of the power consumption concerns, it would not be feasible—or efficient—to continuously collect data from the *Martlet* devices. Instead, a method to trigger data acquisition when a truck is about to cross the bridge has been developed. This feature is accomplished using LIDAR sensors. Two lamp posts precede the bridge, as depicted in the top right of the diagram

in figure 27. The first lamp post, shown in figure 31-A, has one LIDAR sensor interfaced with a *Martlet* and a solar panel and is positioned 10 feet 9 inches above the ground. This height was selected so that trucks would be detected but passenger vehicles would not be. The *Martlet* at this lamp post is constantly reading measurements from the LIDAR sensor; when a truck in either lane is detected, the *Martlet* sends a command to the gateway to notify it to tell the other *Martlets* to start data acquisition.



**A. Far lamp post.**



**B. Lamp post at bridge start.**

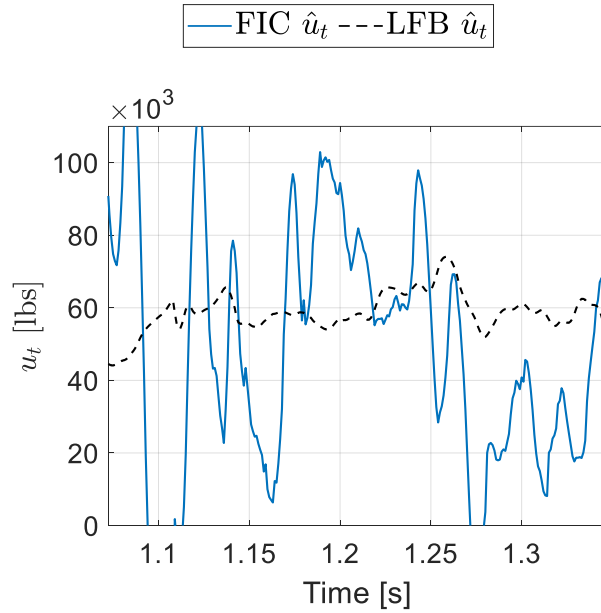
**Figure 31. Photographs. Pole-mounted LIDAR sensors.**

At the lamp post closer to the bridge, shown in figure 31-B, a *Martlet* is interfaced with two LIDAR sensors: one at 10 feet 9 inches and one at ground level. When data acquisition is started, data from both LIDAR sensors is sampled at 1000 Hz. From the upper LIDAR's data, the time that the truck took to travel between the two lamp posts can be used to calculate its speed. From the lower LIDAR's data, the number of wheels of the vehicle can be determined.

## **CONTINUOUS FIELD DATA**

Many trucks have been captured crossing the bridge. Presented here are BWIM results from a typical 18-wheeler truck. The truck crossed the bridge at 7:20 AM on December 16, 2021. It was

travelling at 68 mph in the left lane. The BWIM estimation results for the GVW is shown in figure 32. The period plotted is the time during which all off the axles are on the bridge. For the FIC estimator the GVW estimate is 51,227 lb, and for the LFB estimator the GVW estimate is 55,242 lb.



**Figure 32. Plot. BWIM GVW estimate for unknown truck crossing the bridge.**

## CONCLUSIONS

Thus far, conclusions can be made regarding the sensors to be used and the sensor layout. Based on the control tests, using the strain transducers to detect the truck axles was successful. This approach is more reliable and cost effective than using LIDAR sensors. Furthermore, with transducers placed under each lane, multiple trucks can be detected at one time. This is not possible with just one LIDAR sensor, as it will only measure to the object that is closest to it. This could be an issue if two trucks crossed the bridge at the same time adjacent to each other in different lanes.

From the LS-DYNA BWIM simulations, the layout with sensors at beam quarter points performed the best. However, this results in many sensors on the bridge, increasing the cost, power consumption, and overall complexity of the wireless bridge system implementation. On the other hand, the layout with sensors at beam half points performed well considering the overall error and is a simple and cost-effective layout. Despite this, the time history of the estimation indicated a much less stable estimate, so the accuracy is not as reliable. Ultimately, the layout with the sensors located at beam third points was adopted, since it provided a good compromise of cost and accuracy.

The modal analysis captured the first six modes for the bridge. The experimental mode shapes matched well the finite element model mode shapes; however, there was an initial difference in the natural frequencies. After model updating, the frequencies of the FE model more closely matched those experimentally observed. This updated model was used to perform BWIM for the control truck tests and for unknown trucks crossing the bridge. The control truck test shows GVW estimation errors of less than 10%, and in some cases less than 5%.

## **ACKNOWLEDGEMENTS**

The project team thanks the Georgia Department of Transportation for its support and resources provided to help lead this project to completion. Specifically, we appreciate the technical supervision, feedback, and insights provided by Mr. Rabindra Koirala, as well as the project management and support by Mr. Brennan Roney. In addition, many thanks are owed to those in District 3 who helped make the field installation and testing possible. This includes but is not limited to William Boyd, Jody Evans, Lashanda Bright, and the bucket truck and traffic control crews.



## REFERENCES

1. U.S. Department of Transportation. (2017). *Beyond traffic – trends and choices 2045*. Washington, D.C., USA: <https://apo.org.au/node/122951>
2. Kane, M. *et al.* (2014, April 10). *Development of an extensible dual-core wireless sensing node for cyber-physical systems*. Paper presented at the Proc. SPIE 9061, Sensors and Smart Structures Technologies for Civil, Mechanical, and Aerospace Systems San Diego, CA, USA.
3. Juang, J.-N. and Pappa, R. S. (1985). "An eigensystem realization algorithm for modal parameter identification and model reduction." *Journal of Guidance, Control, and Dynamics*, 8(5), 620-627. doi:10.2514/3.20031
4. Van Overschee, P. and De Moor, B. (1994). "N4SID: Subspace algorithms for the identification of combined deterministic-stochastic systems." *Automatica*, 30(1), 75-93. doi:10.1016/0005-1098(94)90230-5
5. Xia, Y., Chen, B., Weng, S., Ni, Y.-Q., and Xu, Y.-L. (2012). "Temperature effect on vibration properties of civil structures: a literature review and case studies." *Journal of Civil Structural Health Monitoring*, 2(1), 29-46. doi:10.1007/s13349-011-0015-7
6. Chopra, A. K. (2012). *Dynamics of structures: theory and applications to earthquake engineering* (4th ed.). Boston: Prentice Hall.
7. Wang, Y., Dong, X., Li, D., and Otsuki, Y. (2019). SMU: MATLAB Package for Structural Model Updating, version 1.1. Retrieved from <https://github.com/ywang-structures/Structural-Model-Updating>
8. MathWorks Inc. (2020). Optimization Toolbox™ User's Guide. Retrieved from <https://www.mathworks.com/help/optim/>
9. Moses, F. (1979). "Weigh-in-motion system using instrumented bridges." *Transport Eng-J Asce*, 105(3), 233-249.
10. O'Brien, E. J., Rowley, C. W., Gonzalez, A., and Green, M. F. (2009). "A regularised solution to the bridge weigh-in-motion equations." *International Journal of Heavy Vehicle Systems*, 16(3), 310-327. doi:10.1504/ijhvs.2009.027135
11. Law, S. S., Chan, T. H. T., and Zeng, Q. H. (1997). "Moving force identification: A time domain method." *Journal of Sound and Vibration*, 201(1), 1-22. doi:10.1006/jsvi.1996.0774
12. Law, S. S., Chan, T. H. T., and Zeng, Q. H. (1999). "Moving force identification—a frequency and time domains analysis." *Journal of Dynamic Systems, Measurement, and Control*, 121(3), 394-401. doi:10.1115/1.2802487

13. Chan, T. H. T., Law, S. S., Yung, T. H., and Yuan, X. R. (1999). "An interpretive method for moving force identification." *Journal of Sound and Vibration*, 219(3), 503-524. doi:10.1006/jsvi.1998.1904
14. Chen, T. C. and Lee, M. H. (2008). "Research on moving force estimation of the bridge structure using the adaptive input estimation method." *Electronic Journal of Structural Engineering*, 8, 20-28.
15. Wang, H., Nagayama, T., Zhao, B., and Su, D. (2017). "Identification of moving vehicle parameters using bridge responses and estimated bridge pavement roughness." *Engineering Structures*, 153, 57-70. doi:10.1016/j.engstruct.2017.10.006
16. Lalthlamuana, R. and Talukdar, S. (2015). "Obtaining vehicle parameters from bridge dynamic response: a combined semi-analytical and particle filtering approach." *Journal of Modern Transportation*, 23(1), 50-66. doi:10.1007/s40534-014-0065-8
17. Liu, X., Wang, Y., and Verriest, E. I. (2021). "Simultaneous input-state estimation with direct feedthrough based on a unifying MMSE framework with experimental validation." *Mechanical Systems and Signal Processing*, 147, 107083. doi:10.1016/j.ymsp.2020.107083